

1
2 **Uncertainties of satellite-derived surface skin temperatures in the polar oceans: MODIS,**
3 **AIRS/AMSU, and AIRS only**

4
5 Hee-Jung Kang¹, Jung-Moon Yoo^{2*}, Myeong-Jae Jeong³, and Young-In Won⁴

6 ¹Department of Atmospheric Science and Engineering, Ewha Womans University, Seoul 120-750,
7 Republic of Korea

8 ²Department of Science Education, Ewha Womans University, Seoul 120-750, Republic of Korea

9 ³Department of Atmospheric and Environmental Sciences, Gangneung-Wonju National University,
10 Gangneung 210-702, Republic of Korea

11 ⁴Wyle ST&E, NASA/GSFC, Maryland, USA

12
13
14 8 July 2015 (Revised)

15
16
17
18 *Corresponding author

19 Jung-Moon Yoo (yjm@ewha.ac.kr)

20 Department of Science Education
21 Ewha Womans University
22 52, Ewhayeodae-gil, Seodaemun-gu, Seoul 120-750, Korea
23 Office) +82-2-3277-2710, Fax) +82-2-3277-2684

24 Abstract

25 Uncertainties in the satellite-derived Surface Skin Temperature (SST) data in the polar oceans
26 during two periods (April 16-24 and September 15-23) of 2003-2014 were investigated and the three
27 datasets were intercompared as follows: MODerate Resolution Imaging Spectroradiometer Ice
28 Surface Temperature (MODIS IST), the SST of the Atmospheric Infrared Sounder/Advanced
29 Microwave Sounding Unit-A (AIRS/AMSU), and AIRS only. AIRS only algorithm was developed in
30 preparation for the degradation of the AMSU-A. MODIS IST was systematically warmer up to 1.65 K
31 at the sea ice boundary and colder down to -2.04 K in the polar sea ice regions of both the Arctic and
32 Antarctic than that of the AIRS/AMSU. This difference in the results could have been caused by the
33 surface classification method. The spatial correlation coefficient of the AIRS only to the AIRS/AMSU
34 (0.992-0.999) method was greater than that of the MODIS IST to the AIRS/AMSU (0.968-0.994). The
35 SST of the AIRS only compared to that of the AIRS/AMSU had a bias of 0.168 K with a RMSE of
36 0.590 K over the northern hemisphere high latitudes and a bias of -0.109 K with a RMSE of 0.852 K
37 over the southern hemisphere high latitudes. There was a systematic disagreement between the AIRS
38 retrievals at the boundary of the sea ice, because the AIRS only algorithm utilized a less accurate
39 GCM forecast over the seasonally-varying frozen oceans than the microwave data. The three datasets
40 (MODIS, AIRS/AMSU and AIRS only) showed significant warming rates ($2.3 \pm 1.7 \sim 2.8 \pm 1.9$
41 K/decade) in the northern high regions (70-80 N) as expected from the ice-albedo feedback. The
42 systematic temperature disagreement associated with surface type classification had an impact on the
43 resulting temperature trends.

44

45

46 **1. Introduction**

47 The satellite observations of the polar oceans have been more challenging than those of non-frozen
48 ocean and land, because it is more difficult to identify clouds over the various surfaces (Tobin et al.,
49 2006). The surface skin temperature (SST) is one of the most important climate variables that is
50 related to the surface energy balance and the thermal state of the atmosphere (Jin et al., 1997).
51 Compared to ground-based observations, satellite-observed SST data play a crucial role in climate
52 study and model development by providing a uniform resolution data over the globe. The retrievals of
53 AIRS data over the last decade have a significant contribution to various climate studies and model
54 evaluations (Aumann et al., 2003; Tian et al., 2013; Yoo et al., 2013). AIRS retrievals have produced
55 atmospheric temperature, moisture, and ozone profiles on a global scale by the AIRS method itself or
56 together with other instruments (Liu et al., 2008). A lot of comparisons of the AIRS/AMSU data
57 against data from numerical forecast model analysis fields, radiosondes, lidar, and retrievals from
58 high-altitude aircraft have been used to assess the accuracy of the retrievals (Tobin et al., 2006;
59 Susskind et al., 2014). The AIRS retrieval algorithm has been developed and validated gradually with
60 clear sky and clear/cloudy conditions over a non-frozen ocean and then the non-polar land and polar
61 cases (Tobin et al., 2006).

62 The AIRS/AMSU has an advantage of measuring the radiation penetrating through clouds and polar
63 darkness, and has high spectral resolution and coarse spatial resolution (Dong et al., 2006). However,
64 the AIRS only algorithm using only AIRS observations has been developed due to the degradation of
65 the AMSU-A. Microwave and multispectral radiometers were used for global mapping of the sea ice
66 extent and dynamics, while the visible, near-infrared, and infrared sensors could obtain details on the
67 ice concentration, snow/ice albedo, thickness, and IST during clear-sky conditions (Hall et al., 2004;
68 Scott et al., 2014). The MODIS on Earth Observing System (EOS) Aqua, used as infrared
69 measurements, was influenced by water and cloud contamination, but had a higher spatial resolution

70 (Dong et al., 2006). In order to remove the cloud effects in the MODIS IST algorithm, MODIS cloud
71 mask products were used (Hall et al., 2004).

72 Since AIRS and MODIS were co-located on Aqua, they have often been used to make a synergistic
73 algorithm and they have been compared to each other frequently (Molnar and Susskind, 2005; Li et al.,
74 2012; Liu et al., 2014). Li et al. (2012) compared the atmospheric instability from at a single AIRS
75 field of view (FOV; ~13.5 km at nadir) sounding with that of AIRS/AMSU sounding (~45 km),
76 utilizing the MODIS cloud information. Molnar and Susskind (2005) validated the accuracy of the
77 AIRS/AMSU cloud products using MODIS cloud analyses, which have a higher spatial resolution
78 than that of AIRS. Knuteson et al. (2006) compared the MODIS Collection 4 (C4) with the AIRS
79 Version 3 (V3) on the land surface temperature (LST) for the eastern half of the U.S., showing that the
80 monthly differences were approximately 3 K. Lee et al. (2013) investigated the characteristics of the
81 differences between the MODIS land surface skin temperature/sea surface temperature and the
82 AIRS/AMSU surface skin temperature across the globe, and found that the MODIS C5 product was
83 systematically lower by 1.7 K than the AIRS/AMSU V5 product over land in the 50 N-50 S regions,
84 but it was higher by 0.5 K than the AIRS/AMSU product over ocean. Particularly in the sea ice
85 regions, the MODIS annual averages were larger than the AIRS/AMSU values, due to the differential
86 errors in ice/snow emissivity between the retrieval methods (or channels) for the two data products.
87 The differences between the MODIS and AIRS methods were reduced when the MODIS IST and
88 AIRS/AMSU surface skin temperatures were compared for 9-days. The possible reasons for this
89 include the satellite local crossing time (LCT) difference between them due to the different swath
90 width in the high latitude regions, and the emissivity difference between microwave and infrared
91 channels, but more comparison studies are necessary for a longer period to pin down the reasons of
92 such skin temperature discrepancies between MODIS and AIRS/AMSU.

93 The primary purpose of this study was to investigate a relative degree of agreement (or

94 disagreement) among different SST datasets using the MODIS IST C5, the SST of the AIRS/AMSU,
95 and AIRS only V6. The second purpose of this paper was to analyze the temperature trend differences
96 affected by the temperature differences among different data products. The datasets used in this study
97 were described in section 2. In section 3, we compared the MODIS and AIRS only data with the
98 AIRS/AMSU values. We also analyzed the temperature trends from the three satellite-based datasets
99 in section 4, and in the conclusion we summarized our study.

100

101 **2. Data and methods**

102 The Aqua satellite carrying the AIRS, AMSU and MODIS instruments was launched on May 4,
103 2002 with the Earth's Radiant Energy System (CERES), Humidity Sounder for Brazil (HSB) and the
104 Advanced Microwave Scanning Radiometer-EOS (AMSR-E). It has far exceeded its designed life
105 span of 6 years and has a chance of operating into the 2020's (<http://aqua.nasa.gov/>). The Aqua
106 satellite orbits the earth every 98.8 minutes with an equatorial crossing time going north (ascending)
107 at 1:30 p.m. local time (daytime) and going south (descending) at 1:30 a.m. (nighttime) in a sun-
108 synchronous, near polar orbit with an inclination of 98.2° and an operational altitude of 705 km (Tian
109 et al., 2013).

110 As shown in Table 1, we used the datasets of MODIS IST (e.g., Hall et al., 2006) and SSTs of
111 AIRS/AMSU and AIRS only over the northern hemisphere during April 16-24 and over the southern
112 hemisphere on September 15-23 from 2003 to 2014 in order to avoid the polar night when the visible
113 channels of the MODIS did not operate (Hall et al., 2004). The sea surface temperature observed from
114 infrared channels of satellites indicates the values at the skin of sea water, in contrast with the sea
115 surface temperature measured from buoys, of which values represent the temperature of bulk water
116 near the sea surfaces. The infrared sea SST was measured at depths of approximately 10 μm within

117 the oceanic skin layer ($\sim 500 \mu\text{m}$) at the water side of the air-sea interface where the conductive and
118 diffusive heat transfer processes dominated (Emery et al., 2001; Donlon et al., 2002; Liou, 2002).

119 As an imaging spectroradiometer, the MODIS with 36 bands has retrieved various physical
120 parameters such as aerosol optical thickness, land and water surface temperature, leaf area index, and
121 snow cover, etc. (Barnes et al., 1998; Hall and Riggs, 2007). MODIS produced the ‘sea ice by
122 reflectance’ and ‘IST’ in order to identify sea ice (Riggs et al., 1999). The ‘sea ice by reflectance’ was
123 determined by the Normalized Difference Snow Index (NDSI), and the reflectance of Band 1 (0.645
124 μm) and Band 2 (0.858 μm). The NDSI was calculated using Band 4 (0.555 μm) and Band 7 (2.130
125 μm). IST is used as another method for identifying sea ice. The IST derived from the “split-window
126 method” in Eq. (1), where bands 31 and 32 are centered at approximately 11 μm and 12 μm ,
127 respectively. The method was applied in order to identify the ice when the IST was less than 271.5 K.
128 The cutoff temperature between water and ice (271.5 K) may vary depending on the region and
129 season. The IST is calculated as follows:

$$130 \text{ IST} = a + b T_{11} + c (T_{11} - T_{12}) + d [(T_{11} - T_{12})(\sec(\theta) - 1)] \quad (1),$$

131 where T_{11} is the brightness temperature (K) in 11 μm , T_{12} is the brightness temperature (K) in 12 μm ,
132 and θ is the scan angle from nadir. The difference between the T_{11} and the skin temperature from the
133 LOWTRAN can be less than 3 K for a skin temperature between 230 K and 260 K (Key et al., 1997).
134 Since the value of T_{11} itself was a good estimate, coefficients a-d were defined for the following
135 temperature ranges: $T_{11} < 240 \text{ K}$, $240 \text{ K} \leq T_{11} \leq 260 \text{ K}$, and $260 \text{ K} < T_{11}$ (Riggs et al., 2006). The IST
136 algorithm was only applied to the polar ocean pixels that were determined to be clear by the MODIS
137 cloud mask using visible reflectance (Hall et al., 2004). The surface in the IST algorithm was assumed

138 to be snow (Key et al., 1997). MODIS ISTs were provided as daily polar fields with a 4 km by 4 Km
139 resolution.

140 The AIRS spectrometer is a high spectral resolution spectrometer with 2,378 channels in the
141 thermal infrared spectrum and 4 bands in the visible spectrum (Won, 2008). The AIRS and AMSU
142 were coupled in order to play a role as an advanced sounding system under clear and cloudy
143 conditions (Aumann et al., 2003). The AIRS/AMSU algorithm is independent of the GCM, except for
144 the use of GCM surface pressure to determine the bottom boundary conditions (Molnar and Susskind,
145 2005). V6 is the most current retrieval algorithm since the launch of AIRS instrument, and detailed
146 descriptions are given in Olsen (2013b). The primary products from AIRS suite include the
147 atmospheric temperature-humidity profiles, ozone profiles, sea/land surface skin temperature (SST),
148 and cloud related parameters such as the outgoing longwave radiation (OLR) (Susskind et al., 2011).
149 In the AIRS/AMSU algorithm, the surface classification was conducted using the brightness
150 temperature difference in 23 GHz (AMSU ch1) and 50 GHz (AMSU ch3). The difference (brightness
151 temperature at 23 GHz minus brightness temperature at 50 GHz) had a negative value on the sea ice
152 and a positive value on the water (Grody et al., 1999; Hewison and English, 1999). Also, the
153 brightness temperature difference between 23 GHz (AMSU ch1) and 31 GHz (AMSU ch2) could
154 distinguish the age of the sea ice (Kongoli et al., 2008). The accuracy of AIRS/AMSU SST can be
155 affected by surface misclassification, which is caused by the surface emissivity changes, the pixel
156 mixed with the various surface types, and the ice pixel pooled with water.

157 After the surface type classification from the AMSU retrieval, the initial state for atmospheric
158 and surface parameters, cloud parameters and OLR was generated using the Neural Network
159 methodology (Susskind et al., 2011, 2014). The methodology was used to approximate some functions
160 between the input and output vectors by training (Gardner and Dorling, 1998). Next, the initial clear
161 column radiances were generated, which were based on the initial state and the observed infrared

162 radiances. The surface and atmospheric variables, including the surface skin temperature, were
163 retrieved by updating the cloud cleared infrared radiance, iteratively. The cloud properties and
164 outgoing longwave radiation were then retrieved, followed by the error estimates and quality control.
165 In the AIRS only V6, shortwave window region 3.76–4.0 μm was used in order to derive the surface
166 skin temperature and surface spectral emissivity (ϵ).

167 AMSU channels 4-5 had not been available since 2007 and 2010, respectively, due to radiometric
168 noise. In preparation for the degradation of the other AMSU channels, the AIRS only algorithm was
169 developed excluding the AMSU observations. The algorithm was similar to that of AIRS/AMSU, but
170 it did not use the AMSU-A observations in any step of the physical retrieval process and the quality
171 control methodology. The AIRS only algorithm has utilized the forecast surface temperature from the
172 NOAA Global Forecast System (GFS) in order to determine whether the oceanic surface is highly
173 likely to be liquid or frozen, instead of AMSU observations (Olsen, 2013a; Susskind et al., 2014).

174 AIRS/AMSU L2 product (AIRX2RET) is based on 3×3 AIRS FOVs coexisting within a single
175 AMSU footprint, and the horizontal resolution of AIRS and AMSU is approximately 13.5 km and 45
176 km, respectively (Aumann et al., 2002; Zheng et al., 2015). The L2 dataset of AIRS only is provided
177 on 3×3 AIRS FOVs (~45 km) like that of AIRS/AMSU. The two L3 products of the AIRS/AMSU
178 and AIRS only used in this study have also been analyzed under the same spatial resolution of a $1^\circ \times 1^\circ$
179 (~100 km \times 100 km) grid (Table 1).

180 We calculated the climatology and anomaly values from the yearly 9-day mean temperatures in a 1°
181 by 1° grid for the 12-year period of Aqua satellite observations in order to estimate the temperature
182 anomaly trends. The trends of the MODIS IST were derived only when the number of yearly data was
183 at least 10 out of 12 entire years at each grid point. The trends of the AIRS/AMSU and AIRS only
184 were derived only when the number of yearly datasets was 12, covering the entire years of the

185 analysis at each grid. The bootstrap method (Wilks, 1995) was used to calculate at a 95% confidence
186 interval. In the method, 10,000 linear temperature trends were generated by random sampling,
187 allowing repetition of 10,000 yearly anomaly temperature datasets. Then, we estimated the 95%
188 confidence interval of 10,000 temperature trends.

189

190 **3. Comparison of the satellite-derived surface skin temperatures: IST vs SST**

191 Figure 1a shows the spatial coverage and the averaged value of the MODIS IST over the southern
192 hemisphere during September 15-23 of 2003-2014. In order to solve the spatial resolution mismatches,
193 the original resolution of the MODIS data with a 4 km by 4 km grid (Fig. 1a) was re-gridded to a 1°
194 by 1° grid in the case of MODIS data present over 50 % (Fig. 1b). A grid spacing of 1° corresponds to
195 approximately 111 km on the equator, and it becomes reduced poleward. In the zonal averaged SST
196 analysis, this 50% criterion was used. During the same period, the spatial distributions of the
197 climatological T_{skin} (AA_V6) and T_{skin} (AO_V6) were also shown in Fig. 1c-d, respectively. As
198 expected, the MODIS and AIRS showed the spatial distribution of the climatological SST, warmer at
199 the lower latitudes than the higher latitudes. The SST distributions over the northern hemisphere
200 during April 16-24 of 2003-2014 have been shown in Kang and Yoo (2015).

201 Figure 2a displays the number of years when both T_{skin} (MODIS) and T_{skin} (AA_V6) are available at
202 each grid point over the southern hemisphere. The number near 60 S was smaller than that of the other
203 regions because the MODIS IST algorithm only produced its data in the cloud-free pixels. Similar
204 distributions by the clouds were shown in Fig. 2b and 2d for the same reason. The reduced number of
205 observations near 60 S had a spatial distribution similar to that of the frontal cloud bands that were
206 likely associated with the mid-/high-latitude depressions encircling the Antarctica (e.g., Jakob, 1999;
207 Comiso and Stock, 2001; Lachlan-Cope, 2010; Boucher et al., 2013). Figure 2c shows the number of

208 years when both $T_{\text{skin}}(\text{AO_V6})$ and $T_{\text{skin}}(\text{AA_V6})$ were available at each grid. Most of the grids had
209 both $T_{\text{skin}}(\text{AO_V6})$ and $T_{\text{skin}}(\text{AA_V6})$ for a period of more than 10 years.

210 Figure 3a presents the spatial distribution of the temporal difference in a $1^{\circ} \times 1^{\circ}$ grid between the
211 climatological $T_{\text{skin}}(\text{MODIS})$ and $T_{\text{skin}}(\text{AA_V6})$ during April 16-24 of 2003-2014 over the northern
212 hemisphere. In general, $T_{\text{skin}}(\text{MODIS})$ at 60-70 N was higher than the $T_{\text{skin}}(\text{AA_V6})$. $T_{\text{skin}}(\text{MODIS})$
213 was about 3 K higher than the $T_{\text{skin}}(\text{AA_V6})$ on the Hudson Bay and near Greenland, whereas it was
214 about -2 K lower near the center of the Arctic Ocean. The relationship between the climatological T_{skin}
215 (MODIS) and $T_{\text{skin}}(\text{AA_V6})$ was presented in the scatter diagrams (Fig. 3b). The scatter plot revealed
216 a temperature interval which deviated from the simple linear line. The discontinuous shape appeared
217 at the freezing point (~273 K) and the turning point (~260 K) in terms of $T_{\text{skin}}(\text{MODIS})$, changing the
218 coefficient of the MODIS IST algorithm. In the interval, $T_{\text{skin}}(\text{MODIS})$ was systematically higher than
219 the $T_{\text{skin}}(\text{AA_V6})$ in the 260 – 273 K range of $T_{\text{skin}}(\text{MODIS})$. The slope in the range was 0.85, lower
220 than the slope for the whole regression line (0.97). There was a better agreement in the 240-260 K
221 range, where the difference between the T_{11} and the SST in the LOWTRAN was less than 3 K (Key et
222 al., 1997). The better agreement in the range greater than 280K was also shown.

223 Figure 3b was the same as Fig. 3a except for $T_{\text{skin}}(\text{MODIS})$ vs. $T_{\text{skin}}(\text{AO_V6})$. The differences
224 between the two datasets were very similar to those in Fig. 3a. However, $T_{\text{skin}}(\text{MODIS})$ was more
225 than 4 K higher than $T_{\text{skin}}(\text{AO_V6})$ in some regions near the Greenland and the Barents Sea. The
226 slope (0.93) in the 260 – 273 K range of $T_{\text{skin}}(\text{MODIS})$ also indicated a deviation from the total slope
227 (0.98) in the scatter plot (Fig. 3d), similar to that in Fig. 3b. Figure 3e showed the difference between
228 $T_{\text{skin}}(\text{AO_V6})$ to $T_{\text{skin}}(\text{AA_V6})$. Overall, the agreement was much better than the previous two cases
229 (Fig. 3a and c), except for in the Greenland Sea, the Barents Sea, and the Okhotsk Sea. Both T_{skin}
230 (AO_V6) and $T_{\text{skin}}(\text{AA_V6})$ agreed with each other ($r=0.999$) well except for near the freezing point.

231 Figure 4 showed discrepancies among the three types of SST datasets over the southern hemisphere
232 during September 15-23 of 2003-2014. It has been noted that there was a latitudinal band encircling
233 Antarctica at 60-70 S, where $T_{\text{skin}}(\text{MODIS})$ was higher than both the $T_{\text{skin}}(\text{AA_V6})$ and $T_{\text{skin}}(\text{AO_V6})$
234 (Fig. 4a and c). The circular region corresponded to the sea ice/water boundary which was expected to
235 move seasonally. This implies a systematic difference between $T_{\text{skin}}(\text{MODIS})$ and $T_{\text{skin}}(\text{AA_V6})$ in
236 the sea ice classification. The corresponding scatter plots also revealed a discontinuous (i.e., not linear)
237 shape in the 260 – 273 K range of $T_{\text{skin}}(\text{MODIS})$ (Fig. 4b and d). The slopes in that range were 0.84-
238 0.94, which were smaller than the slope (0.98) in the whole range. In addition, $T_{\text{skin}}(\text{MODIS})$ showed
239 lower temperature values than $T_{\text{skin}}(\text{AA_V6})$ and $T_{\text{skin}}(\text{AO_V6})$ near the Antarctic peninsula, in the
240 region from Weddell Sea to Ross Sea (Fig. 4a and c).

241 The comparison between two types of AIRS datasets also showed the circular pattern around
242 Antarctica where $T_{\text{skin}}(\text{AO_V6})$ was lower by 1.5-5.6 K than $T_{\text{skin}}(\text{AA_V6})$ (Fig. 4e). The discrepancy
243 near the sea ice/water boundary was clear, possibly due to the difference in the sea ice detection
244 method between the two datasets. The uncertainty of the SST at the sea ice boundary was
245 distinguished from the other regions. Both $T_{\text{skin}}(\text{AO_V6})$ and $T_{\text{skin}}(\text{AA_V6})$ were in good agreement,
246 other than the sea ice/water boundary regions. The scatter pattern of the $T_{\text{skin}}(\text{AA_V6})$ versus that of
247 the $T_{\text{skin}}(\text{AO_V6})$ showed that the two datasets generally agreed with each other, but the disagreement
248 near the freezing point again occurred indicating a cold bias of AIRS only with respect to
249 AIRS/AMSU (Fig. 4f).

250 Figure 5 showed the annual-average spatial distributions for $T_{\text{skin}}(\text{MODIS})$ minus $T_{\text{skin}}(\text{AA_V6})$ in
251 the southern hemisphere from September 15-23 of 2003-2014. Although the 9-day composite values
252 were used in each year, $T_{\text{skin}}(\text{MODIS})$ data did not exist in some areas. It was because the MODIS
253 IST algorithm was valid only for cloud-free pixels. The systematic positive values at the boundary of
254 the sea ice consistently occurred, while the negative ones occurred on some areas of the sea ice near

255 Antarctica every year.

256 Figure 6 presented the interannual variation of the spatial distribution of $T_{\text{skin}}(\text{AO_V6})$ minus $T_{\text{skin}}(\text{AA_V6})$ for the study period. As already seen in Fig. 4e, the values of $T_{\text{skin}}(\text{AO_V6})$ compared to
257 $T_{\text{skin}}(\text{AA_V6})$ show systematic negative values encircling Antarctica during the period. In addition,
258 there were positive values over the sea-ice prevailing areas inside the circle, with the location varying
259 from year to year, which must be related to the difference in the surface type characterization.
260

261 Table 2 showed the statistics of bias, spatial correlation coefficient (r), and root mean square error
262 (RMSE) obtained from the 12-year climatologies of 2003-2014 in order to analyze the systematic
263 error among the three types of satellite-observed temperatures quantitatively. This analysis for each
264 hemispheric vernal period has been performed over the two regions (35-90 N, 60-90 N) of the
265 northern hemisphere during April 16-24, and over the regions (40-90 S, 60-90 S) of the southern
266 hemisphere during September 15-23. The spatial correlation coefficient between the two satellite data
267 sets was computed in this study as follows; i) The climatological 9-day composite data of SSTs
268 during 2003-2014 were computed in a $1^{\circ} \times 1^{\circ}$ grid of the two data sets, respectively. ii) We
269 computed the spatial correlation coefficient between the two datasets, using their climatological
270 values in a $1^{\circ} \times 1^{\circ}$ grid within a given latitude band. The values in parentheses indicated the average
271 obtained from the statistics for each year and their corresponding standard deviations. Based on the
272 climatology values, the SST of the AIRS retrievals were comparable with respect to the $T_{\text{skin}}(\text{MODIS})$
273 ($r=0.959-0.994$). $T_{\text{skin}}(\text{MODIS})$ tended to systematically exceed the AIRS retrievals over the polar
274 oceans (bias = 0.198-0.597 K). Hall et al. (2004) reported the accuracy of $T_{\text{skin}}(\text{MODIS})$ with the bias
275 values of 1.2-1.3 K near the South Pole and the Arctic Ocean. The RMSE of 1.847 K for $T_{\text{skin}}(\text{MODIS})$
276 vs. the $T_{\text{skin}}(\text{AA_V6})$ over 60-90 S in our study was slightly higher than that in the study of Hall et al.
277 (2004).

278 From the intercomparison of the three datasets, the bias (-0.109-0.597) and RMSE (0.590-2.173)
279 over the high latitude belt (60-90 N and S) tended to be larger, and the correlation coefficients
280 ($r=0.959-0.986$) was smaller than those over 35-90 N and 40-90 S among the three comparisons
281 (Table 2). This result indicated that there was more disagreement over the high latitudes than over
282 other regions. The spatial correlation coefficient (0.992-0.999) between T_{skin} (AO_V6) and T_{skin}
283 (AA_V6) was greater than those (0.968-0.994) between T_{skin} (MODIS) and T_{skin} (AA_V6). In the high
284 latitudes T_{skin} (AO_V6) with respect to T_{skin} (AA_V6) had a positive bias of 0.168 K with a RMSE of
285 0.590 K in the northern hemisphere, but a bias of -0.109 K with a RMSE of 0.852 K in the southern
286 hemisphere. The high correlations ($r = 0.998-0.999$) between the AIRS/AMSU and AIRS only (i.e.,
287 AIRS retrievals) over the 35-90 N and 40-90 S areas showed that the AIRS only can be a good
288 alternative for the AIRS/AMSU, except for at the region of the sea ice boundary ($r = 0.992$ over the
289 60-90 S). The disagreement between T_{skin} (AA_V6) and T_{skin} (AO_V6) at the region where the sea ice
290 and water mixed appeared, because the AIRS only used less accurate GCM forecast data for surface
291 classification over the potentially frozen oceans.

292 Figure 7 presents the zonal mean temperature difference among the three satellite-observed datasets
293 in a $1^{\circ} \times 1^{\circ}$ grid over the northern hemisphere during April 16–24 of 2003-2014 and over the
294 southern hemisphere during September 15-23, 2003-2014. The red, blue and green lines represent the
295 zonally averaged annual values of T_{skin} (MODIS) minus T_{skin} (AA_V6), T_{skin} (MODIS) minus T_{skin}
296 (AO_V6), and T_{skin} (AO_V6) minus T_{skin} (AA_V6), respectively. The climatological annual values
297 have been calculated from the interannually-varying yearly data, shown in Fig. 8. The black dashed
298 line, the difference between the original MODIS IST data (4km x 4km) and converted T_{skin} (MODIS)
299 ($1^{\circ} \times 1^{\circ}$) indicated the possible error from the conversion of spatial resolution. The differences by the
300 conversion over both hemispheres were within 0.3 K and 0.5 K, respectively. The original T_{skin}
301 (MODIS), converted T_{skin} (MODIS), T_{skin} (AA_V6), and T_{skin} (AO_V6) were chosen under the same

302 condition in space and time, and each grid ($1^\circ \times 1^\circ$) of a degree latitudinal band.

303 It is hard to see in Fig. 3a the systematic difference due to the sea ice detection over the northern
304 hemisphere because of the continental distribution. However, Fig. 7 clearly showed that the difference
305 among the T_{skin} (MODIS), T_{skin} (AA_V6), and T_{skin} (AO_V6) existed over the northern hemisphere.
306 T_{skin} (MODIS) was warmer than T_{skin} (AA_V6) in 56-81 N and 54-69 S, while cooler than T_{skin} (AA_V6)
307 in the other latitudinal zone. It has been noted that the peak of the difference between T_{skin} (MODIS)
308 and two AIRS datasets in the northern hemisphere high-latitude region took place in a broader region
309 than in the southern hemisphere. T_{skin} (MODIS) was up to 1.65 K higher than the AIRS datasets at the
310 boundaries of the sea ice/water, whereas it was lower by up to -2.04 K over the sea ice region. The
311 MODIS IST algorithm was the optimized on the snow/ice surface type, and thus the underestimation
312 of T_{skin} (MODIS) in the 35-54 N and 40-55 S may not be unexpected. In general, the overestimation of
313 T_{skin} (MODIS) to the AIRS retrievals occurred at the sea ice boundary and the underestimation
314 occurred in the sea ice region that can be covered with snow/ice.

315 The grey solid lines in Fig. A1a-b mean the 5% significance level of the differences between T_{skin}
316 (T_{skin} (MODIS) and T_{skin} (AA_V6), and between T_{skin} (AO_V6) and T_{skin} (AA_V6) over a possibly frozen
317 region (poleward from 50 N and 50 S, respectively). Based on the *t*-test (von Storch and Zwiers, 1999)
318 at significance level of $p < 0.05$, the temperature disagreement between T_{skin} (MODIS) and T_{skin}
319 (AA_V6) (red solid line) is significant in 50-55 N, 58-70 N, 89-90 N, 50-53 S, and 57-62 S (Fig. A1a).
320 Considering the uncertainty of MODIS due to the conversion of spatial resolution (black dashed line),
321 the temperature disagreement in 57-62 S can become insignificant. However, the discrepancy in 58-70
322 N is significant even if the uncertainty of MODIS is considered. The difference between T_{skin} (AO_V6)
323 and T_{skin} (AA_V6) in 53-60 S is significant (Fig. A1b).

324 The color-coded lines in Fig. 8 interannually represent the differences in temperature among the

325 three datasets for individual years. The thick black lines indicated the yearly difference averages.
326 There existed a significant degree of interannual variation in the difference between T_{skin} (MODIS)
327 and the two AIRS datasets (Fig. 8a-b). The variation was larger in 2009, 2010 and 2011 over the
328 regions northward of 60 N and southward of 55 S where sea ice existed. Figure 8b shows a value of
329 T_{skin} (MODIS) minus T_{skin} (AO_V6) that was similar to that in Fig. 8a. T_{skin} (MODIS) was lower than
330 T_{skin} (AO_V6) at the ice surface, but higher than T_{skin} (AO_V6) at the boundary of the sea ice. Figure
331 8c showed the interannual variation of T_{skin} (AO_V6) minus T_{skin} (AA_V6). The interannual variation
332 of the difference between the AIRS retrievals was much larger in the high latitude than in the mid-
333 latitudes. The maximum difference of 1.56 K between the AIRS retrievals was found at 87-88 N in
334 2011.

335 There could be several reasons for the observed differences between T_{skin} (MODIS) and T_{skin}
336 (AA_V6). The main one can be attributed to the difference in the channel used for the retrievals of the
337 skin temperature. The AIRS/AMSU V6 only utilized shortwave window channels for the surface skin
338 temperature, while the MODIS IST algorithm used the longwave window regions. The shortwave
339 window could be mixed with the solar radiation during the daytime, but it was suitable for
340 temperature sounding (Chahine, 1975, 1977; Susskind et al., 2014). The advantage of the longwave
341 window was that its range corresponded to the peak of the infrared radiation emitted from the earth
342 (Prakash, 2000). On the other hand, the longwave window radiation could be affected more by clouds.
343 In order to avoid cloud contamination, the MODIS IST algorithm analyzed the pixel when the
344 MODIS cloud mask was reported as clear sky (Hall et al., 2004). The MODIS cloud mask using
345 visible reflectance had a high accuracy during the daytime, but a lower accuracy during the nighttime
346 due to low illumination. As another reason for the temperature difference, Lee et al. (2013) suggested
347 that there were substantial differences in LCT between MODIS and AIRS in the high latitude regions,
348 since the different scan angles of the two instruments resulted in different footprints, which could lead

349 to the observed difference in temperature. However, we suggested that the surface type classification
350 method could be the primary reason for the temperature difference between the MODIS-based and
351 AIRS-based datasets. AIRS/AMSU SST was retrieved after the surface type was classified. On the
352 other hand, the MODIS IST was calculated without the surface type classification step. Then, the
353 MODIS algorithm categorized pixels being ice if IST was less than the cutoff temperature. MODIS
354 IST was calculated on the snow, sea ice, and ocean, assuming the surface was snow-covered (sea ice).
355 The IST was utilized as a criterion for identifying the ice/water which might cause significant
356 disagreement between the T_{skin} (MODIS) and T_{skin} (AA_V6) in the range of 260-273 K.

357

358 **4. Comparison of the surface skin temperature trends: IST vs SST**

359 In order to further investigate the effects of the difference among the satellite-observed
360 temperatures from different measurement techniques or algorithms on the temperature anomaly trend,
361 we calculated the trend in some latitude belts, using the three satellite-observed temperature datasets
362 at each grid during April 16-24 of 2003-2014 (in the northern hemisphere) and September 15-23 of
363 2003-2014 in the southern hemisphere. During this period, an unusually extensive surface melting
364 event was observed in 2012 (Nghiem et al., 2012; Hall et al., 2013; Comiso and Hall, 2014).

365 Table 3 shows the temperature anomaly trend with a 95% confidence level on the 10° latitude belt.
366 We arranged the data of MODIS IST, AIRS/AMSU, and AIRS only under the same condition in space
367 and time. The significant warming trend in $70\text{-}80^{\circ}$ N was estimated in the following order:
368 AIRS/AMSU (2.83 K/decade) $>$ AIRS only (2.71 K/decade) $>$ T_{skin} (MODIS) (2.30 K/decade). The
369 warming (0.10 to 0.38 K/decade) at $40\text{-}50^{\circ}$ N and $50\text{-}60^{\circ}$ S, and the cooling (-0.08 to -1.94 K/decade) at
370 $80\text{-}90^{\circ}$ N, $60\text{-}70^{\circ}$ N, $50\text{-}60^{\circ}$ N, $60\text{-}70^{\circ}$ S and $70\text{-}80^{\circ}$ S of the three datasets occurred, but the trends were
371 not significant. Comiso and Hall (2014) reported the SST trend using the Goddard Institute for Space

372 Studies (GISS) dataset as 0.60 K/decade and the trend using the Advanced Very High Resolution
373 Radiometer (AVHRR) dataset as 0.69 K/decade in the Arctic (> 64 N) during 1981-2012. Our result in
374 70-80 N, compared with the above studies, seems to indicate an acceleration in the Arctic warming.

375 The warming trend in the northern hemispheric high latitudes had been known to be caused in part
376 by the well-known positive feedback among snow/ice, surface albedo and temperature (Curry et al.,
377 1995; Comiso and Hall, 2014). T_{skin} (MODIS) had a greater cooling tendency compared to T_{skin}
378 (AA_V6) in the higher latitude regions (70-90 N and 60-80 S) (Table 3). The trend difference between
379 the two temperatures was -0.69 K/decade at 70-80 S. The trend difference of the T_{skin} (AA_V6) and
380 T_{skin} (AO_V6) (i.e., AIRS only minus AIRS/AMSU) was the largest (-0.26 K/decade) at 60-70 N. The
381 cooling trend (-0.90 K/decade) of the T_{skin} (AO_V6) was greater than that (-0.65 K/decade) of T_{skin}
382 (AA_V6) at the latitude band.

383 Figure 9a-b showed the SST anomaly trends from the T_{skin} (MODIS) in a 1° by 1° grid over the
384 northern hemisphere during April 16-24 of 2003-2014 and over the southern hemisphere during
385 September 15-23 of 2003-2014. The T_{skin} (MODIS) trend was calculated on the grid, which had
386 available data that existed for over 10 years. Figure 9c-d and Fig. 9e-f showed the trend data for T_{skin}
387 (AA_V6) and T_{skin} (AO_V6), respectively, which all had 12-year data, individually. The trend
388 distributions in all three of the datasets were similar over the northern hemisphere. Warming trend in
389 the Beaufort Sea, East Siberian Sea and Kara Sea was detected, while cooling was observed in the
390 Hudson Bay and near Greenland. The significant warming trend appeared at 70-80 N as shown in
391 Table 3, and the trend based on the spatial distribution varied depending on the regions (Fig. 9a, c and
392 e). According to Comiso and Hall (2014), a strong warming trend (> 1.5 K/decade) existed near the
393 Kara Sea and Baffin Bay among the entire Arctic, consistent with the noticeable trend revealed near
394 the Kara Sea in our study. Over the southern hemisphere, there were not enough data to derive a trend
395 for T_{skin} (MODIS) mostly due to clouds. The trend analysis over the sea ice regions from T_{skin} (AA_V6)

396 and $T_{\text{skin}}(\text{AO_V6})$ showed a strong cooling trend, especially near the Antarctic peninsula between the
397 Weddell and Ross Seas (Fig. 9d and f). The cooling trend was generally dominant over the southern
398 hemisphere. Marshall et al. (2015) suggested that based on the model experiments, the cooling trend
399 around Antarctica as opposed to the warming trend around the Arctic Ocean was the result of the
400 offset between the greenhouse gas and ozone hole responses, emphasizing the larger cooling effects
401 associated with the Antarctic ozone hole.

402 The 12-year mean of the $T_{\text{skin}}(\text{MODIS})$ minus $T_{\text{skin}}(\text{AA_V6})$ (Fig. 10a and c) and of the trend
403 difference between $T_{\text{skin}}(\text{MODIS})$ and $T_{\text{skin}}(\text{AA_V6})$ (Fig. 10b and d) were compared in order to
404 reveal the relationship between the temperature difference and the corresponding trend difference over
405 the northern hemisphere during April 16-24 of 2003-2014 and over the southern hemisphere during
406 September 15-23 of 2003-2014. $T_{\text{skin}}(\text{MODIS})$ was higher than $T_{\text{skin}}(\text{AA_V6})$ over the bays of
407 Hudson and Baffin, and Bering Sea (Fig. 10a). The warming trend of the $T_{\text{skin}}(\text{MODIS})$ was also
408 greater than that of the $T_{\text{skin}}(\text{AA_V6})$ over the Hudson Bay and near the Kara Sea (Fig. 10b). The data
409 for the trend difference in the southern hemisphere was not sufficient due to the missing data of
410 $T_{\text{skin}}(\text{MODIS})$ in the cloudy condition (Fig. 10d).

411 Figure 11 showed over both hemispheres the 12-year mean of the $T_{\text{skin}}(\text{AO_V6})$ minus T_{skin}
412 (AA_V6) (Fig. 11a and c) and the corresponding trend difference of the $T_{\text{skin}}(\text{AO_V6})$ and T_{skin}
413 (AA_V6) (Fig. 11b and d). The relationship of the temperature difference and trend difference over
414 the southern hemisphere in Fig. 10 was hard to analyze due to the absence of a $T_{\text{skin}}(\text{MODIS})$ trend
415 (Fig. 10c-d). However, Fig. 11c-d clearly showed that the temperature difference had a significant
416 impact on the trend difference over the southern hemisphere. The trend of the $T_{\text{skin}}(\text{AA_V6})$ and T_{skin}
417 (AO_V6) agreed well except for at the region of the sea ice boundary, implying that the algorithm
418 identifying the sea ice affected the SST trend.

419 Uncertainties among satellite observations (T_{skin} (MODIS), T_{skin} (AA_V6), and T_{skin} (AO_V6)) in
420 the sea ice region of the northern hemisphere are generally similar to those of the southern hemisphere
421 in terms of zonal averages. However, the systematic difference between the observations can be more
422 clearly seen in the latter region than in the former region due to more oceanic regions in the southern
423 hemisphere (Figs. 10-11, and see also Fig. 7).

424 Table 4 quantitatively showed how the temperature differences among the three types of SST
425 affected each trend difference over the hemispheric regions poleward either from 50 N (shown in the
426 left side of the table) during April 16-24 of 2003-2014 or from 50 S during September 15-23 of 2003-
427 2014. In the upper portion, the average of the temperature difference and the trend difference in the
428 grid corresponding to the temperature difference condition was used, whereas the average values on
429 the grids that had the same signs for the temperature difference and the trend difference were used in
430 the lower portion. Only the cases where grid number was greater than 100 were considered. The
431 warmer temperature led to relatively warming trend, the cooler temperature led to relatively cooling
432 trend. When the T_{skin} (MODIS) was greater than T_{skin} (AA_V6) in the regions poleward from 50 S, the
433 trend difference was in the reduced cooling trend (i.e., warmer direction) as -0.96, -0.66, and -0.21
434 K/decade with the conditions of T_{skin} (MODIS) minus T_{skin} (AA_V6) rising as more than 1 K, 1.5 K,
435 and 2 K, respectively. The uncertainty of the satellite-derived temperatures had a substantial effect on
436 the uncertainty of the temperature trends. The data set has been reduced in the lower section of Table
437 4. The sample size can affect the estimated impact of ΔT on ΔTrend , but it looks like that the impact
438 on the trends in the lower section is almost consistent with that in the upper section despite the
439 reduced sample sizes.

440

441

442 **5. Conclusions**

443 The satellite-derived L3 products of MODIS IST and two SSTs from AIRS/AMSU and AIRS only
444 were investigated with a comparative analysis during the vernal periods of 2003-2014: April 16-24
445 over the northern hemisphere and September 15-23 over the southern hemisphere. The original
446 MODIS IST data were regridded onto a $1^\circ \times 1^\circ$ grid box for comparison with the AIRS retrievals. The
447 difference between the original MODIS IST and the converted one was within 0.5 K in a latitudinal
448 belt.

449 The differences among the three types of satellite derived SST data were most prominent over the
450 sea ice regions. T_{skin} (MODIS) and T_{skin} (AA_V6) were comparable ($r=0.97-0.99$), but there existed
451 systematic disagreement occurred in the T_{skin} (MODIS) range of 260-273 K. The southern hemispheric
452 high latitude (60 S-90 S) was the primary contributor to the disagreement between them. In
453 comparison with the T_{skin} (AA_V6) in a latitudinal belt, the T_{skin} (MODIS) was higher by up to 1.65 K
454 than T_{skin} (AA_V6) on the boundary of the sea ice/water, whereas it was lower by up to -2.04 K in the
455 sea ice region.

456 The spatial correlation coefficients (0.992-0.999) of the T_{skin} (AO_V6) and T_{skin} (AA_V6) over both
457 hemispheres were greater than those (0.968-0.994) between T_{skin} (MODIS) and T_{skin} (AA_V6). The
458 T_{skin} (AO_V6) compared to the T_{skin} (AA_V6) had a bias of 0.168 K with a RMSE of 0.590 K over the
459 northern hemisphere high latitudes and a bias of -0.109 K with a RMSE of 0.852 K over the southern
460 hemispheric high latitudes. There was a systematic disagreement between the T_{skin} (AA_V6) and T_{skin}
461 (AO_V6) at the sea ice boundary. It is likely due to the fact that the AIRS only algorithm utilized a
462 less accurate GCM forecast than the microwave data over the seasonally-varying frozen oceans.

463 The temperature differences among the three types of datasets showed a high degree of interannual
464 variations over the latitudinal belts where sea ice existed. The significant warming rates ($2.3 \pm 1.7 \sim$

465 2.8 ± 1.9 K/decade) were revealed by all three datasets in the northern hemispheric high-latitude
466 regions (70-80 N) could be interpreted as the ice-albedo feedback. The discrepancies between the
467 trends of the T_{skin} (AA_V6) and T_{skin} (AO_V6) occurred at the sea ice boundary. When the T_{skin}
468 (AA_V6) trends were compared to those of the T_{skin} (MODIS) or T_{skin} (AO_V6) in a $1^\circ \times 1^\circ$ grid, the
469 warmer temperature difference tended to lead to a relative warming trend, whereas the cooler
470 temperature difference tended to lead to a relative cooling trend.

471 The systematic disagreement between the T_{skin} (MODIS) and T_{skin} (AA_V6) could be caused by (1)
472 the channels used for the surface skin temperature, (2) the cloud contamination, (3) the LCT
473 difference between the MODIS and AIRS, and (4) the surface type classification method. Whereas the
474 AIRS/AMSU V6 used only the shortwave window channels for the surface skin temperature, MODIS
475 IST used the longwave window regions. The MODIS IST product utilized the MODIS cloud mask
476 with visible reflectance, which had lower accuracy during the night (Hall et al., 2004). Lee et al.,
477 (2013) reported that the LCTs between the MODIS and AIRS were almost the same from 60 N-60 S,
478 but they were quite different in the high latitude regions. It is likely that the main cause to the
479 observed SST differences near the sea ice boundary was in the way the surface type was classified.
480 The AIRS/AMSU algorithm conjugated the emissivity difference in the low and high frequency
481 microwave bands (23 and 50 GHz) in order to identify sea ice. However, MODIS IST was calculated
482 without the surface type classification.

483 The AIRS/AMSU L2 data offer the surface type (coastline, land, ocean, two types of sea ice, two
484 types of snow, and glacier/snow), and the AIRS/AMSU L3 data provide the number of these various
485 surface types in a grid. The AIRS only L2 also offer the surface type (coastline, land, ocean, two types
486 of sea ice, and snow), and its L3 data provide the number of these various surface types in a grid.
487 Under the condition without ground truth, the direct validation has a limit because the surface
488 classifications of AIRS/AMSU and AIRS only have some difference. Although the AIRS only has

489 utilized the forecast surface temperature from the GFS, there is a good agreement in SST between
490 AIRS/AMSU and AIRS only in most regions. However, the disagreement between them over the land
491 regions of the Sahara desert, parts of Spain and in the US with snow cover at night has been reported
492 (Dang et al., 2012).

493 We have investigated the effect in the difference of spatial resolution between L2 and L3 products,
494 utilizing the L2 products (T_{skin} (MODIS), T_{skin} (AA_V6), and T_{skin} (AO_V6)) for a year of 2003.
495 Overall the uncertainties among the three L2 datasets are similar to those of the L3, but the magnitude
496 of T_{skin} (MODIS) minus T_{skin} (AA_V6) for L2 datasets is somewhat different from that for the L3
497 datasets (not shown). Based on the L3 products in this study, it seems to be sufficient to allow us to
498 show the systematic characteristics of the uncertainties. Although the detailed analysis of L2 is
499 beyond the scope of this study, further studies are warranted.

500 The SST in the polar region is a useful parameter being used to derive the climate change signal,
501 although it has been challenging to measure an accurate SST. Based on our results from detailed
502 comparative investigation, we cautiously suggested that the observed difference and uncertainty
503 among the satellite-derived SSTs were likely caused by the different sea ice detecting methods used in
504 each algorithm. This study suggested that the ice forecast derived from other microwave satellite data
505 could improve the AIRS only product from the better accuracy of surface classification. In addition,
506 the methods also affected the temperature trend. In this study, we aimed to help in understanding
507 characteristics of the infrared and microwave measurements for the surface skin temperature, and the
508 method for identifying sea ice. We believe the results of this study can be useful for the interpretation
509 and the modeling of the climate change associated with the temperature trends.

510

511

512 Acknowledgements

513 This study was supported by the National Research Foundation of Korea (NRF) grant funded by the
514 Korean Government (MSIP) (NO. 2009-0083527) and the Korean Ministry of Environment as the
515 Eco-technopia 21 project (NO. 201200016003). We thank Goddard Earth Sciences Data Information
516 and Services Center for AIRS/AMSU data, and NASA National Snow and Ice Data Center for
517 MODIS IST data. We also thank Drs. Bob Iacovazzi, Jr., J. M. Blaisdell, and C.-Y. Liu for their
518 constructive comments.

519 **6. References**

520

521 Aumann, H. H., Chahine, M. T., Gautier, C., Goldberg, M. D., Kalnay, E., McMillin, L. M.,
522 Revercomb, H., Rosenkranz, P. W., Smith, W. L., Staelin, D. H., Strow, L. L., and Susskind, J.:
523 AIRS/AMSU/HSB on the Aqua mission: Design, science objectives, data products, and processing
524 systems, *IEEE Trans. Geosci. Remote Sensing*, 41, 253-264, doi:10.1109/tgrs.2002.808356, 2003.

525 Barnes, W. L., Pagano, T. S., and Salomonson, V. V.: Prelaunch characteristics of the Moderate
526 resolution Imaging Spectroradiometer (MODIS) on EOS-AM1, *IEEE Trans. Geosci. Remote Sensing*,
527 36, 1088-1100, doi:10.1109/36.700993, 1998.

528 Boucher, O., Randall, D., Artaxo, P., Bretherton, C., Feingold, G., Forster, P., Kerminen, V.-M.,
529 Kondo, Y., Liao, H., Lohmann, U., Rasch, P., Sathesh, S. K., Sherwood, S., Stevens, B., and Zhang,
530 X. Y.: Clouds and Aerosols. In: *Climate change 2013: The physical science basis. Contribution of*
531 *working group I to the fifth assessment report of the intergovernmental panel on climate change*,
532 Cambridge University Press, Cambridge, UK, 2013.

533 Chahine, M. T.: Remote sounding of cloudy atmospheres. I. The single cloud layer, *Journal of the*
534 *Atmospheric Sciences*, 31, 233-243, doi:10.1175/1520-0469(1974)031<0233:RSOCAL>2.0.CO;2,
535 1974.

536 Chahine, M. T.: Remote sounding of cloudy atmospheres. II. Multiple cloud formations, *Journal of the*
537 *Atmospheric Sciences*, 34, 744-757, doi:10.1175/1520-0469(1977)034<0744:RSOCAL>2.0.CO;2,
538 1977.

539 Comiso, J. C., and Hall, D. K.: Climate trends in the Arctic as observed from space, *Wiley Interdiscip.*
540 *Rev.-Clim. Chang.*, 5, 389-409, doi:10.1002/wcc.277, 2014.

541 Comiso, J. C., and Stock, L. V.: Studies of Antarctic cloud cover variability from 1982 through 1999,
542 Geoscience and Remote Sensing Symposium, 2001. IGARSS '01. IEEE 2001 International, 1782-
543 1785, 2001.

544 Curry, J. A., Schramm, J. L., and Ebert, E. E.: Sea ice-albedo climate feedback mechanism, *J. Clim.*, 8,
545 240-247, doi:10.1175/1520-0442(1995)008<0240:SIACFM>2.0.CO;2, 1995.

546 Dang, H. V. T., Lambrigtsen, B., and Manning, E.: AIRS/AMSU/HSB version 6 level 2 performance
547 and test report, available at: http://disc.sci.gsfc.nasa.gov/AIRS/documentation/v6_docs/v6releasedocs-1/V6_L2_Performance_and_Test_Report.pdf, last access: 8 June 2015, 2012.

549 Dong, S. F., Gille, S. T., Sprintall, J., and Gentemann, C.: Validation of the Advanced Microwave
550 Scanning Radiometer for the Earth Observing System (AMSR-E) sea surface temperature in the
551 southern ocean, *J. Geophys. Res.-Oceans*, 111, 16, doi:10.1029/2005jc002934, 2006.

552 Donlon, C. J., Minnett, P. J., Gentemann, C., Nightingale, T. J., Barton, I. J., Ward, B., and Murray, M.
553 J.: Toward improved validation of satellite sea surface skin temperature measurements for climate
554 research, *J. Clim.*, 15, 353-369, doi:10.1175/1520-0442(2002)015<0353:tivoss>2.0.co;2, 2002.

555 Emery, W. J., Castro, S., Wick, G. A., Schluessel, P., and Donlon, C.: Estimating sea surface
556 temperature from infrared satellite and in situ temperature data, *Bull. Amer. Meteorol. Soc.*, 82, 2773-
557 2785, doi:10.1175/1520-0477(2001)082<2773:esstfi>2.3.co;2, 2001.

558 Gardner, M. W., and Dorling, S. R.: Artificial neural networks (the multilayer perceptron) - A review
559 of applications in the atmospheric sciences, *Atmos. Environ.*, 32, 2627-2636, doi:10.1016/s1352-
560 2310(97)00447-0, 1998.

561 Grody, N., Weng, F., and Ferraro, R.: Application of AMSU for obtaining water vapor, cloud liquid
562 water, precipitation, snow cover and sea ice concentration, in: Technical proceedings of the tenth
563 international atovs study conference, Colorado, USA, 27 January - 2 February 1999, 230-240, 1999.

564 Hall, D. K., and Riggs, G. A.: Accuracy assessment of the MODIS snow products, *Hydrol. Process.*,
565 21, 1534-1547, doi:10.1002/hyp.6715, 2007.

566 Hall, D. K., Key, J. R., Casey, K. A., Riggs, G. A., and Cavalieri, D. J.: Sea ice surface temperature
567 product from MODIS, *IEEE Trans. Geosci. Remote Sensing*, 42, 1076-1087,
568 doi:10.1109/tgrs.2004.825587, 2004.

569 Hall, D. K., Salomonson, V. V., and Riggs, G. A.: MODIS/Aqua Sea Ice Extent and IST Daily L3
570 Global 4km EASE-Grid Day. Version 5. Boulder, Colorado, USA: National Snow and Ice Data Center,
571 2006.

572 Hall, D. K., Comiso, J. C., DiGirolamo, N. E., Shuman, C. A., Box, J. E., and Koenig, L. S.:
573 Variability in the surface temperature and melt extent of the Greenland ice sheet from MODIS,
574 *Geophys. Res. Lett.*, 40, 2114-2120, doi:10.1002/grl.50240, 2013.

575 Hewison, T. J., and English, S. J.: Airborne retrievals of snow and ice surface emissivity at millimeter
576 wavelengths, *IEEE Trans. Geosci. Remote Sensing*, 37, 1871-1879, doi:10.1109/36.774700, 1999.

577 Jakob, C.: Cloud cover in the ECMWF reanalysis, *J. Clim.*, 12, 947-959, doi:10.1175/1520-
578 0442(1999)012<0947:cciter>2.0.co;2, 1999.

579 Jin, M., Dickinson, R. E., and Vogelmann, A. M.: A comparison of CCM2–BATS skin temperature
580 and surface-air temperature with satellite and surface observations, *J. Clim.*, 10, 1505-1524,
581 doi:10.1175/1520-0442(1997)010<1505:ACOCBS>2.0.CO;2, 1997.

582 Kang, H.-J., and Yoo, J.-M.: Uncertainties of satellite-observed surface skin temperatures due to sea
583 ice in the Arctic ocean: MODIS, AIRS/AMSU and AIRS Only, *J. Korean Earth Sci. Soc.*, 36, 139-157,
584 doi:10.5467/JKESS.2015.36.2.139, 2015 (in Korean).

585 Key, J. R., Collins, J. B., Fowler, C., and Stone, R. S.: High-latitude surface temperature estimates
586 from thermal satellite data, *Remote Sens. Environ.*, 61, 302-309, doi:10.1016/S0034-4257(97)89497-
587 7, 1997.

588 Knuteson, R., Cychosz, J., Lee, S. C., Revercomb, H., Tobin, D., and Vinson, K.: Comparison of LST
589 from AIRS and MODIS from the EOS Aqua platform, 10th symposium on Integrated Observing and
590 Assimilation Systems for the Atmosphere, Oceans, and Land Surface (IOASAOLS), the 86th AMS
591 annual meeting, 2006.

592 Kongoli, C., Boukabara, S., Yan, B., Weng, F., and Ferraro, R.: Sea ice concentration retrievals from
593 variationally retrieved microwave surface emissivities, available at:
594 http://microrad2008.cetem.org/public/presentations/20080314_16.50_Kongoli.pdf, last access: 4
595 December 2014, 2008.

596 Lachlan-Cope, T.: Antarctic clouds, *Polar Res.*, 29, 150-158, doi:10.1111/j.1751-8369.2010.00148.x,
597 2010.

598 Lee, Y.-R., Yoo, J.-M., Jeong, M.-J., Won, Y.-I., Hearty, T., and Shin, D.-B.: Comparison between
599 MODIS and AIRS/AMSU satellite-derived surface skin temperatures, *Atmos. Meas. Tech.*, 6, 445-455,
600 doi:10.5194/amt-6-445-2013, 2013.

601 **Li, J., Liu, C. Y., Zhang, P., and Schmit, T. J.: Applications of full spatial resolution space-based
602 advanced infrared soundings in the preconvective environment, *Wea. Forecasting*, 27, 515-524, doi:
603 10.1175/WAF-D-10-05057.1, 2012.**

604 Liou, K. N.: An introduction to atmospheric radiation, Academic Press, Amsterdam; Boston:, 2002.

605 Liu, C. Y., Li, J., Weisz, E., Schmit, T. J., Ackerman, S. A., and Huang, H. L.: Synergistic use of AIRS
606 and MODIS radiance measurements for atmospheric profiling, *Geophys. Res. Lett.*, 35, 6,
607 doi:10.1029/2008gl035859, 2008.

608 **Liu, C. Y., Liu, G. R., Lin, T. H., Liu, C. C., Ren, H., and Young, C. C.: Using surface stations to**

609 improve sounding retrievals from hyperspectral infrared instruments, *IEEE Trans. Geosci. Remote*
610 *Sensing*, 52, 6957-6963, doi: 10.1109/tgrs.2014.2305992, 2014.

611 Marshall, J., Armour, K. C., Scott, J. R., Kostov, Y., Hausmann, U., Ferreira, D., Shepherd, T. G., and
612 Bitz, C. M.: The ocean's role in polar climate change: asymmetric Arctic and Antarctic responses to
613 greenhouse gas and ozone forcing, *Phil. Trans. R. Soc.*, 372, 20130040, doi: 10.1098/rsta.2013.0040,
614 2014.

615 Molnar, G. I., and Susskind, J.: Validation of AIRS/AMSU cloud retrievals using MODIS cloud
616 analyses, in: *Proc. SPIE 5806, Algorithms and Technologies for Multispectral, Hyperspectral, and*
617 *Ultraspectral Imagery XI*, 13 July 2005, 618-629, 2005.

618 Nghiem, S. V., Hall, D. K., Mote, T. L., Tedesco, M., Albert, M. R., Keegan, K., Shuman, C. A.,
619 DiGirolamo, N. E., and Neumann, G.: The extreme melt across the Greenland ice sheet in 2012,
620 *Geophys. Res. Lett.*, 39, 6, doi:10.1029/2012gl053611, 2012.

621 Olsen, E.: AIRS/AMSU/HSB version 6 changes from version 5, available at:
622 http://disc.sci.gsfc.nasa.gov/AIRS/documentation/v6_docs/v6releasedocs-1/V6_Changes_from_V5.pdf, last access: 4 December 2014, 2013a.

624 Olsen, E.: AIRS/AMSU/HSB version 6 retrieval flow, available at:
625 http://disc.sci.gsfc.nasa.gov/AIRS/documentation/v6_docs/v6releasedocs-1/V6_Retrieval_Flow.pdf,
626 last access: 4 December 2014, 2013b.

627 Prakash, A.: Thermal remote sensing: concepts, issues and application, *XIXth ISPRS Congress*,
628 Amsterdam, Netherlands, 239-243, 2000.

629 Riggs, G. A., Hall, D. K., and Ackerman, S. A.: Sea ice extent and classification mapping with the
630 Moderate resolution Imaging Spectroradiometer airborne simulator, *Remote Sens. Environ.*, 68, 152-
631 163, doi:10.1016/s0034-4257(98)00107-2, 1999.

632 Riggs, G. A., Hall, D. K., and Salomonson, V. V.: MODIS sea ice products user guide to collection 5,
633 available at: http://modis-snow-ice.gsfc.nasa.gov/uploads/siug_c5.pdf, last access: 7 February 2015,
634 2006.

635 Scott, K. A., Li, E., and Wong, A.: Sea ice surface temperature estimation using MODIS and AMSR-E
636 data within a guided variational model along the Labrador Coast, *IEEE J. Sel. Top. Appl. Earth*
637 *Observ. Remote Sens.*, 7, 3685-3694, doi:10.1109/jstars.2013.2292795, 2014.

638 Susskind, J., Blaisdell, J. M., Iredell, L., and Keita, F.: Improved temperature sounding and quality
639 control methodology using AIRS/AMSU Data: The AIRS science team version 5 retrieval algorithm,
640 *IEEE Trans. Geosci. Remote Sensing*, 49, 883-907, doi:10.1109/tgrs.2010.2070508, 2011.

641 Susskind, J., Blaisdell, J. M., and Iredell, L.: Improved methodology for surface and atmospheric
642 soundings, error estimates, and quality control procedures: the atmospheric infrared sounder science
643 team version-6 retrieval algorithm, *APPRES*, 8, 084994, doi:10.1117/1.JRS.8.084994, 2014.

644 Tian, B. J., Fetzer, E. J., Kahn, B. H., Teixeira, J., Manning, E., and Hearty, T.: Evaluating CMIP5
645 models using AIRS tropospheric air temperature and specific humidity climatology, *J. Geophys. Res.-*
646 *Atmos.*, 118, 114-134, doi:10.1029/2012jd018607, 2013.

647 Tobin, D. C., Revercomb, H. E., Knuteson, R. O., Lesht, B. M., Strow, L. L., Hannon, S. E., Feltz, W.
648 F., Moy, L. A., Fetzer, E. J., and Cress, T. S.: Atmospheric radiation measurement site atmospheric
649 state best estimates for atmospheric infrared sounder temperature and water vapor retrieval validation,
650 *J. Geophys. Res.-Atmos.*, 111, 18, doi:10.1029/2005jd006103, 2006.

651 von Storch, H. and Zwiers, F. W.: *Statistical Analysis in Climate Research*, Cambridge University
652 Press, Cambridge, UK, 1999.

653 Wilks, D. S.: *Statistical methods in the atmospheric sciences*, Academic Press, San Diego:, 1995.

654 Won, Y.-I.: Readme document for AIRS Level-3 version 5 standard products: daily (AIRH3STD,
655 AIRX3STD, AIRS3STD), 8-day (AIRH3ST8, AIRX3ST8, AIRS3ST8) & monthly (AIRH3STM,
656 AIRX3STM, AIRS3STM), available at:
657 <http://disc.sci.gsfc.nasa.gov/TRMM/AIRS/documentation/readmes/README.AIR-3ST.pdf>, last
658 access: 4 December 2014, 2008.

659 Yoo, J.-M., Won, Y.-I., Jeong, M.-J., Kim, K.-M., Shin, D.-B., Lee, Y.-R., and Cho, Y.-J.: Intensity of
660 climate variability derived from the satellite and MERRA reanalysis temperatures: AO, ENSO, and
661 QBO, *J. Atmos. Sol.-Terr. Phys.*, 95-96, 15-27, doi:10.1016/j.jastp.2013.01.002, 2013.

662 **Zheng, J., Li, J., Schmit, T., Li, J., and Liu, Z.: The impact of AIRS atmospheric temperature and
663 moisture profiles on hurricane forecasts: Ike (2008) and Irene (2011), *Adv. Atmos. Sci.*, 32, 319-335,
664 doi: 10.1007/s00376-014-3162-z, 2015.**

665 Table 1. The information on the satellite-observed surface skin temperature (T_{skin}) Level 3 (L3) data used in this study. Three datasets of T_{skin} were compared
 666 over the northern hemisphere during April 16-24 of 2003-2014, and over the southern hemisphere during September 15-23 of 2003-2014. The abbreviations
 667 used in this table are as follows: temp (temperature), IST (ice surface skin temperature), OBS (observation), and SFC (surface).

Satellite-observed dataset	Version (Collection)	Temp type	Area	Spatial resolution	Number of OBS	Satellite sensor	Abbreviation	Reference
MODIS IST	MYD29E1D/5	Skin	Polar ocean	4km×4km	1/day	Aqua MODIS	$T_{\text{skin}}(\text{MODIS})$	Hall et al.(2004)
AIRS/AMSU SFC skin temp	AIRX3STD/6	Skin	Globe	1°×1°	2/day	Aqua AIRS/AMSU-A	$T_{\text{skin}}(\text{AA_V6})$	Susskind et al. (2014)
AIRS only SFC skin temp	AIRS3STD/6	Skin	Globe	1°×1°	2/day	Aqua AIRS	$T_{\text{skin}}(\text{AO_V6})$	Susskind et al. (2014)

668
 669
 670
 671
 672
 673
 674
 675
 676
 677
 678

679 Table 2. Statistical comparisons of the climatological 9-day composite data during 2003-2014 over both hemispheres; $T_{\text{skin}}(\text{MODIS})$ vs. $T_{\text{skin}}(\text{AA_V6})$, $T_{\text{skin}}(\text{MODIS})$ vs.
 680 $T_{\text{skin}}(\text{AO_V6})$, and $T_{\text{skin}}(\text{AO_V6})$ vs. $T_{\text{skin}}(\text{AA_V6})$. The values in this table were calculated based on the 12-year composite mean values. The values in parentheses indicate
 681 the 12-year mean values and their standard deviations during 2003-2014. Bias: $T_{\text{skin}}(\text{MODIS})$ minus $T_{\text{skin}}(\text{AA_V6})$, $T_{\text{skin}}(\text{MODIS})$ minus $T_{\text{skin}}(\text{AO_V6})$, and $T_{\text{skin}}(\text{AO_V6})$
 682 minus $T_{\text{skin}}(\text{AA_V6})$, r: correlation coefficient, RMSE: root mean square error.

Region	$T_{\text{skin}}(\text{MODIS})$ vs. $T_{\text{skin}}(\text{AA_V6})$			$T_{\text{skin}}(\text{MODIS})$ vs. $T_{\text{skin}}(\text{AO_V6})$			$T_{\text{skin}}(\text{AO_V6})$ vs. $T_{\text{skin}}(\text{AA_V6})$		
	Bias (K)	r	RMSE (K)	Bias (K)	r	RMSE (K)	Bias (K)	R	RMSE (K)
35-90N	-0.169 (-0.161±0.231)	0.994 (0.990±0.002)	1.491 (1.909±0.156)	-0.289 (-0.324±0.308)	0.993 (0.990±0.003)	1.563 (1.963±0.260)	0.133 (0.137±0.130)	0.999 (0.997±0.001)	0.574 (1.018±0.131)
40-90S	0.026 (-0.010±0.218)	0.989 (0.982±0.003)	1.480 (2.082±0.144)	0.203 (0.035±0.282)	0.985 (0.980±0.003)	1.756 (2.184±0.119)	-0.141 (-0.139±0.079)	0.998 (0.994±0.001)	0.750 (1.272±0.092)
60-90N	0.223 (0.194±0.357)	0.986 (0.973±0.009)	1.501 (1.986±0.227)	0.597 (-0.013±0.475)	0.986 (0.972±0.011)	1.591 (2.033±0.370)	0.168 (0.170±0.214)	0.998 (0.992±0.003)	0.590 (1.027±0.216)
60-90S	0.198 (0.368±0.537)	0.968 (0.906±0.023)	1.847 (2.871±0.276)	0.306 (0.295±0.620)	0.959 (0.898±0.021)	2.173 (2.987±0.271)	-0.109 (-0.108±0.142)	0.992 (0.976±0.005)	0.852 (1.498±0.112)

683

684

685

686

687

688 Table 3. The rate of the surface skin temperature change (K/decade) of the MODIS, AIRS/AMSU, and AIRS only in each 10° latitudinal belt over the northern hemisphere
689 (NH) during April 16-24 and over the southern hemisphere (SH) during September 15-23 of 2003-2014, using their colocated data in a 1°×1° grid. The ± values define the 95%
690 confidence intervals for the trends. The symbol ‘*’ means the significant value at a 95% confidence interval. Note that the rates are subject to large uncertainty due to the
691 short periods of the satellite-based temperature records.

Latitudinal belt	MODIS	AIRS/AMSU	AIRS only	MODIS minus AIRS/AMSU	MODIS minus AIRS only	AIRS only minus AIRS/AMSU
<NH>						
80-90 N	-0.558±3.101	-0.100±3.673	-0.093±3.736	-0.458	-0.465	0.007
70-80 N	2.302±1.701*	2.826±1.878*	2.711±1.788*	-0.524	-0.409	-0.115
60-70 N	-0.506±1.173	-0.646±1.294	-0.902±1.050	0.140	0.396	-0.256
50-60 N	-0.345±0.539	-0.522±0.628	-0.466±0.550	0.177	0.121	0.056
40-50 N	0.292±0.402	0.103±0.576	0.191±0.565	0.189	0.101	0.088
<SH>						
50-60 S	0.375±0.400	0.315±0.466	0.316±0.600	0.060	0.059	0.001
60-70 S	-1.944±2.271	-1.304±1.890	-1.300±1.918	-0.640	-0.644	0.004
70-80 S	-0.769±2.687	-0.081±2.586	-0.135±2.633	-0.688	-0.634	-0.054

692
693
694
695
696
697
698
699
700
701
702

703 Table 4. Uncertainties of the satellite-derived surface skin temperature rate (or trend; ΔTrend) due to the temperature difference (ΔT_{skin}) for the cases of T_{skin} (MODIS) minus
 704 T_{skin} (AA_V6) and T_{skin} (AO_V6) minus T_{skin} (AA_V6) in the upper portion of the table. Also, the values of uncertainties provided in the lower portion of the table indicate the
 705 cases of $\pm\Delta\text{Trend}$ with respect to $\pm\Delta T_{\text{skin}}$ (double signs in the same order). The uncertainties are not shown when the number of the grid ($1^\circ \times 1^\circ$ points (i.e., No. of grids in
 706 the table) is less than 100.

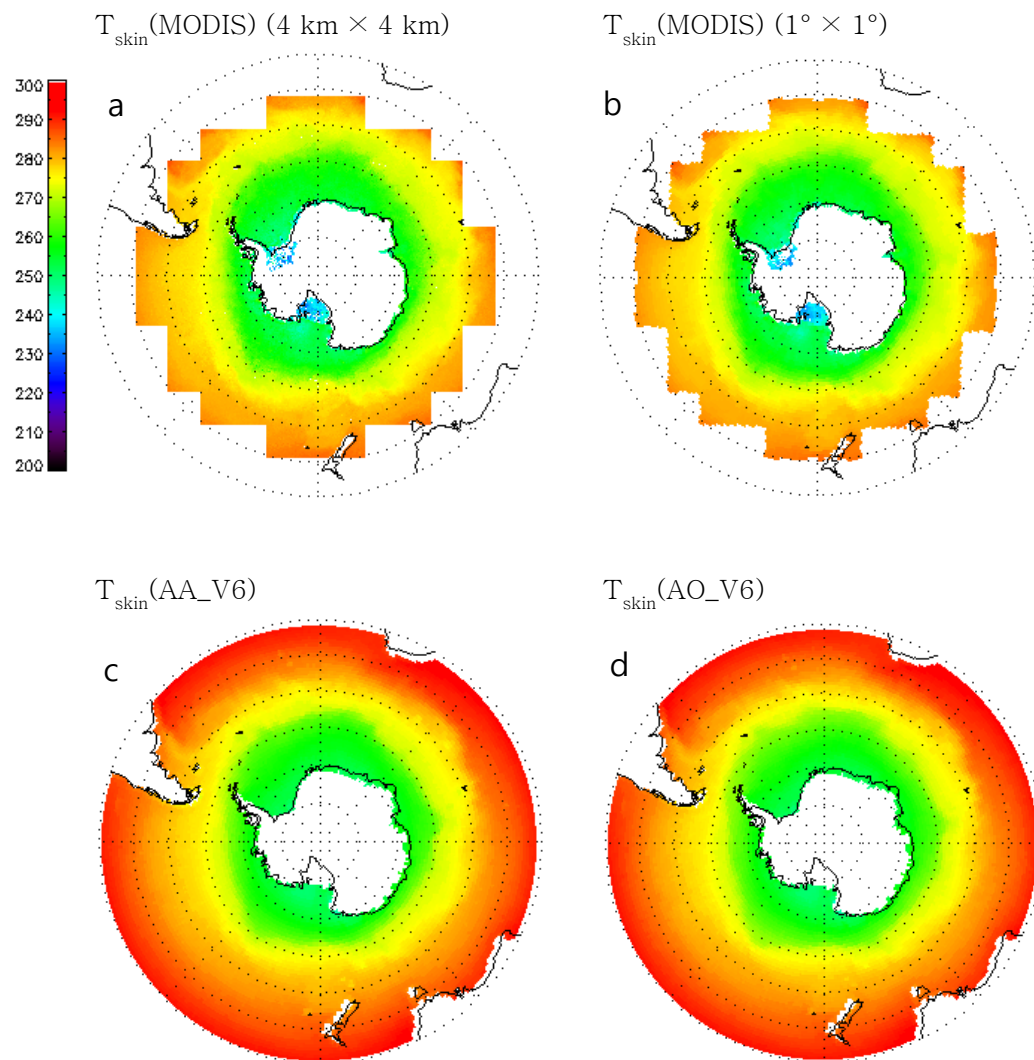
707

ΔT_{skin} (K)	Poleward from 50N						Poleward from 50S					
	T_{skin} (MODIS) vs. T_{skin} (AA_V6)			T_{skin} (AO_V6) vs. T_{skin} (AA_V6)			T_{skin} (MODIS) vs. T_{skin} (AA_V6)			T_{skin} (AO_V6) vs. T_{skin} (AA_V6)		
	No. of grids	ΔT_{skin}	ΔTrend (K/decade)	No. of grids	ΔT_{skin}	ΔTrend (K/decade)	No. of grids	ΔT_{skin}	ΔTrend (K/decade)	No. of grids	ΔT_{skin}	ΔTrend (K/decade)
≥ 1.0	2155	2.01	-0.10	95	-	-	425	2.01	-0.96	378	1.37	0.03
≥ 1.5	1506	2.34	0.04	19	-	-	253	2.25	-0.66	104	1.80	0.24
≥ 2.0	940	2.71	0.19	5	-	-	134	2.69	-0.21	22	-	-
≤ -1.0	1839	-1.59	-0.45	236	-2.25	-0.34	224	-1.71	-0.43	877	-2.19	-0.37
≤ -1.5	921	-1.94	-0.45	162	-2.72	-0.47	115	-2.18	-0.16	654	-2.52	-0.55
≤ -2.0	367	-2.27	-0.60	109	-3.20	-0.78	55	-	-	472	-2.82	-0.69
<hr/>												
≥ 1.0	912	2.15	1.21	40	-	-	139	2.09	1.36	179	1.40	1.01
≥ 1.5	707	2.41	1.22	8	-	-	94	-	-	51	-	-
≥ 2.0	499	2.70	1.22	1	-	-	64	-	-	15	-	-
≤ -1.0	1309	-1.59	-0.90	126	-2.51	-2.02	122	-1.69	-2.42	500	-2.26	-1.96
≤ -1.5	643	-1.96	-0.92	89	-	-	61	-	-	387	-2.55	-2.06
≤ -2.0	272	-2.28	-1.02	69	-	-	27	-	-	293	-2.81	-2.06

708

709

Sep 15-23, 2003-2014



710

711 Fig. 1. (a) 12-year composite skin temperatures (K) of the MODIS IST over the southern hemisphere during
712 September 15-23 of 2003-2014. The original MODIS data (MYD29E1D) have a $4 \text{ km} \times 4 \text{ km}$ spatial resolution.
713 Their spatial resolution has been reconstructed to $1^\circ \times 1^\circ$ in Fig. 1b in order to compare this data with the
714 AIRS/AMSU data. Figure 1c-d is the surface skin temperatures of the AIRS/AMSU and AIRS only over the
715 southern hemisphere ocean during September 15-23 of 2003-2014, respectively.

716

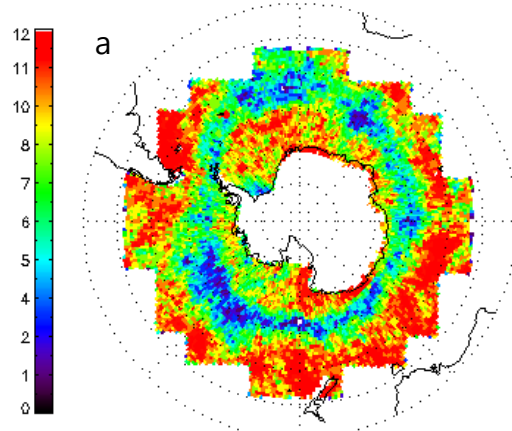
717

718

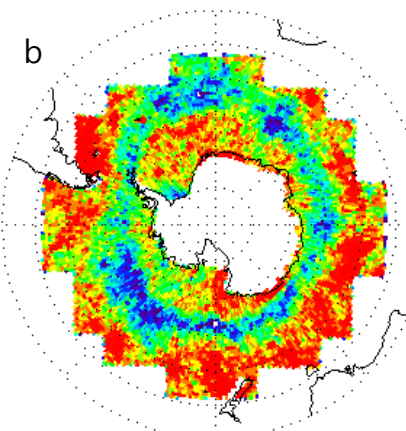
719

Sep 15–23, 2003–2014

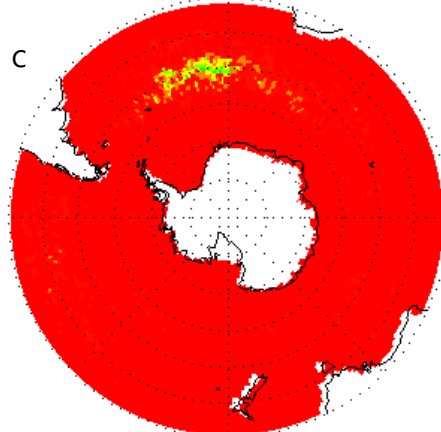
$T_{\text{skin}}(\text{MODIS})$ & $T_{\text{skin}}(\text{AA_V6})$



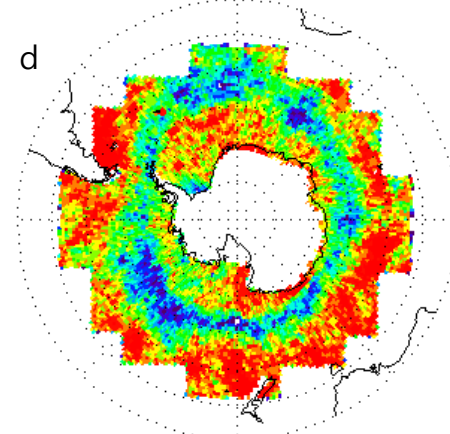
$T_{\text{skin}}(\text{MODIS})$ & $T_{\text{skin}}(\text{AO_V6})$



$T_{\text{skin}}(\text{AO_V6})$ & $T_{\text{skin}}(\text{AA_V6})$



$T_{\text{skin}}(\text{MODIS})$ & $T_{\text{skin}}(\text{AA_V6})$ & $T_{\text{skin}}(\text{AO_V6})$



720

721 Fig. 2. The number of co-located observations of (a) $T_{\text{skin}}(\text{MODIS})$ and $T_{\text{skin}}(\text{AA_V6})$, (b) $T_{\text{skin}}(\text{MODIS})$ and
722 $T_{\text{skin}}(\text{AO_V6})$, and (c) $T_{\text{skin}}(\text{AO_V6})$ and $T_{\text{skin}}(\text{AA_V6})$ over the southern hemisphere during September 15-23
723 of 2003-2014. (d) Same as in Fig. 2c except for three different datasets ($T_{\text{skin}}(\text{MODIS})$, $T_{\text{skin}}(\text{AA_V6})$, and $T_{\text{skin}}(\text{AO_V6})$).
724

725

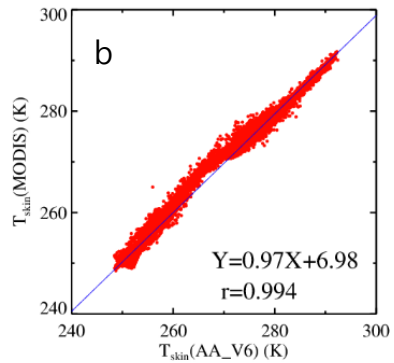
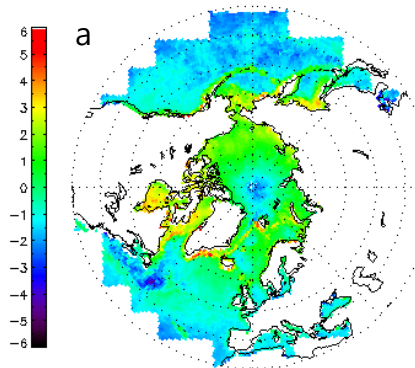
726

727

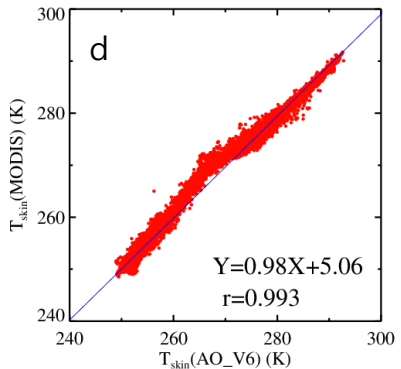
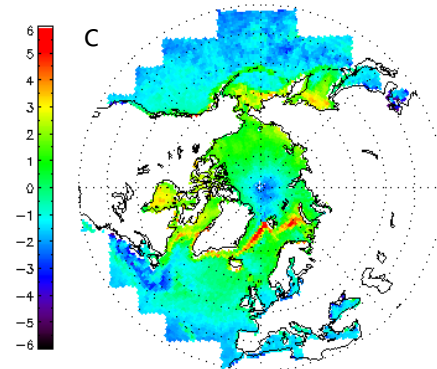
728

729

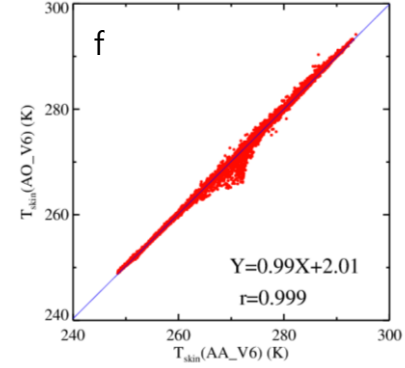
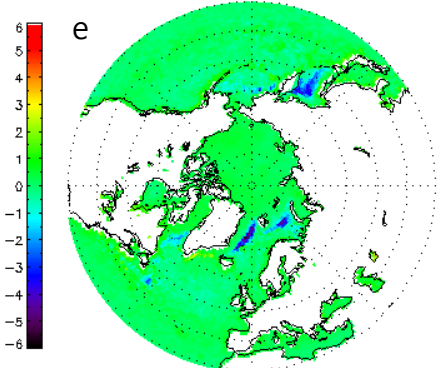
$T_{\text{skin}}(\text{MODIS})$ minus $T_{\text{skin}}(\text{AA_V6})$



$T_{\text{skin}}(\text{MODIS})$ minus $T_{\text{skin}}(\text{AO_V6})$



$T_{\text{skin}}(\text{AO_V6})$ minus $T_{\text{skin}}(\text{AA_V6})$

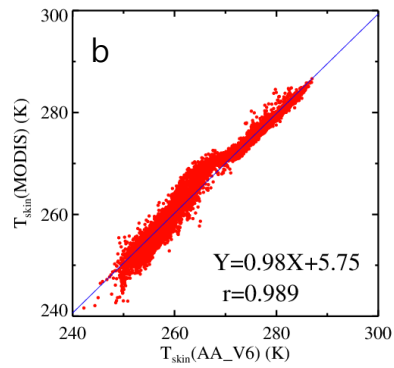
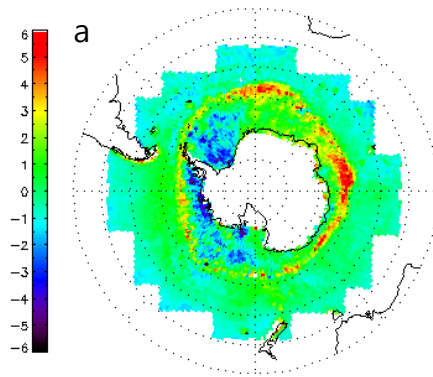


730

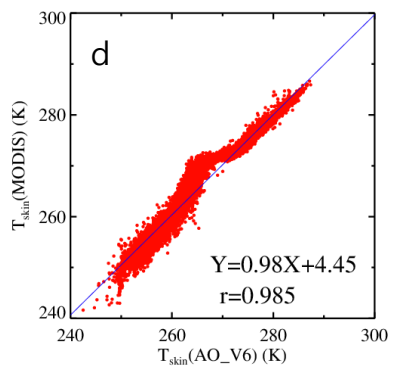
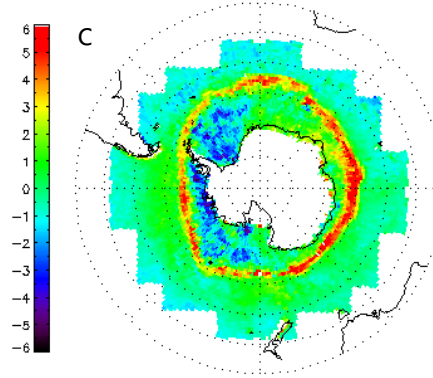
731 Fig. 3. The distributions of (a) $T_{\text{skin}}(\text{MODIS})$ minus $T_{\text{skin}}(\text{AA_V6})$, (c) $T_{\text{skin}}(\text{MODIS})$ minus $T_{\text{skin}}(\text{AO_V6})$, and (e) $T_{\text{skin}}(\text{AO_V6})$ minus $T_{\text{skin}}(\text{AA_V6})$ over the northern hemisphere during April 16-24 of 2003-2014. The scatter plots of (b) $T_{\text{skin}}(\text{MODIS})$ versus $T_{\text{skin}}(\text{AA_V6})$, (d) $T_{\text{skin}}(\text{MODIS})$ versus $T_{\text{skin}}(\text{AO_V6})$, and (f) $T_{\text{skin}}(\text{AO_V6})$ versus $T_{\text{skin}}(\text{AA_V6})$.

735

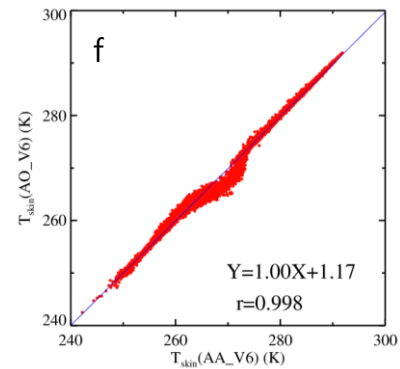
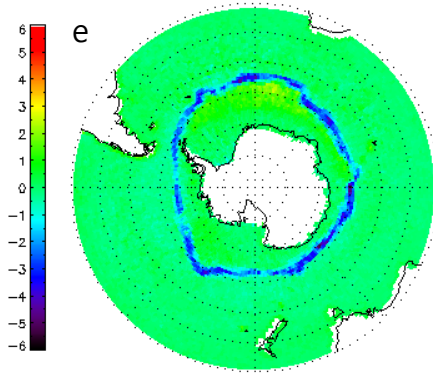
$T_{\text{skin}}(\text{MODIS})$ minus $T_{\text{skin}}(\text{AA_V6})$



$T_{\text{skin}}(\text{MODIS})$ minus $T_{\text{skin}}(\text{AO_V6})$



$T_{\text{skin}}(\text{AO_V6})$ minus $T_{\text{skin}}(\text{AA_V6})$



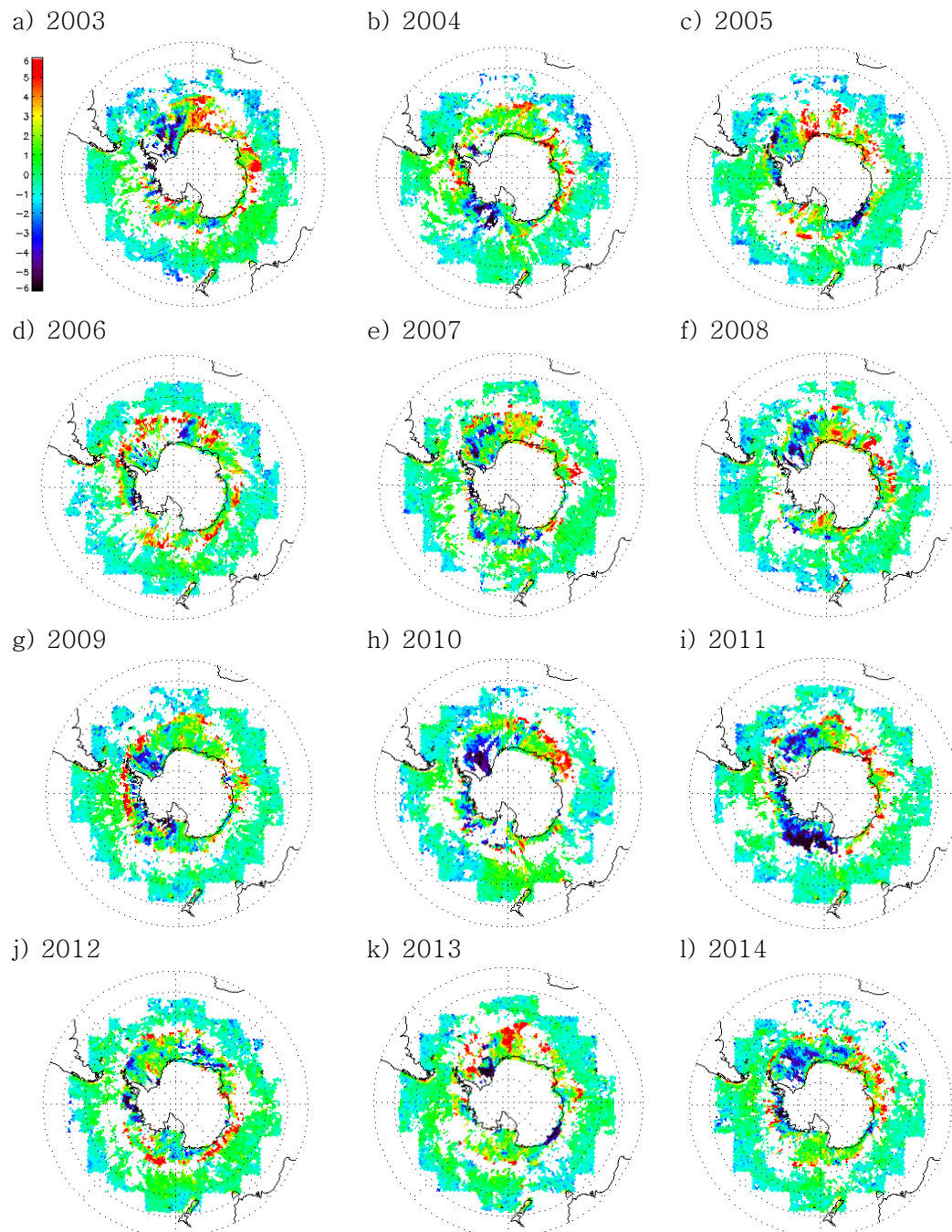
736

737 Fig. 4. Same as in Fig. 3 except for the data taken during September 15-23 of 2003-2014, over the
738 southern hemisphere.

739

740

741

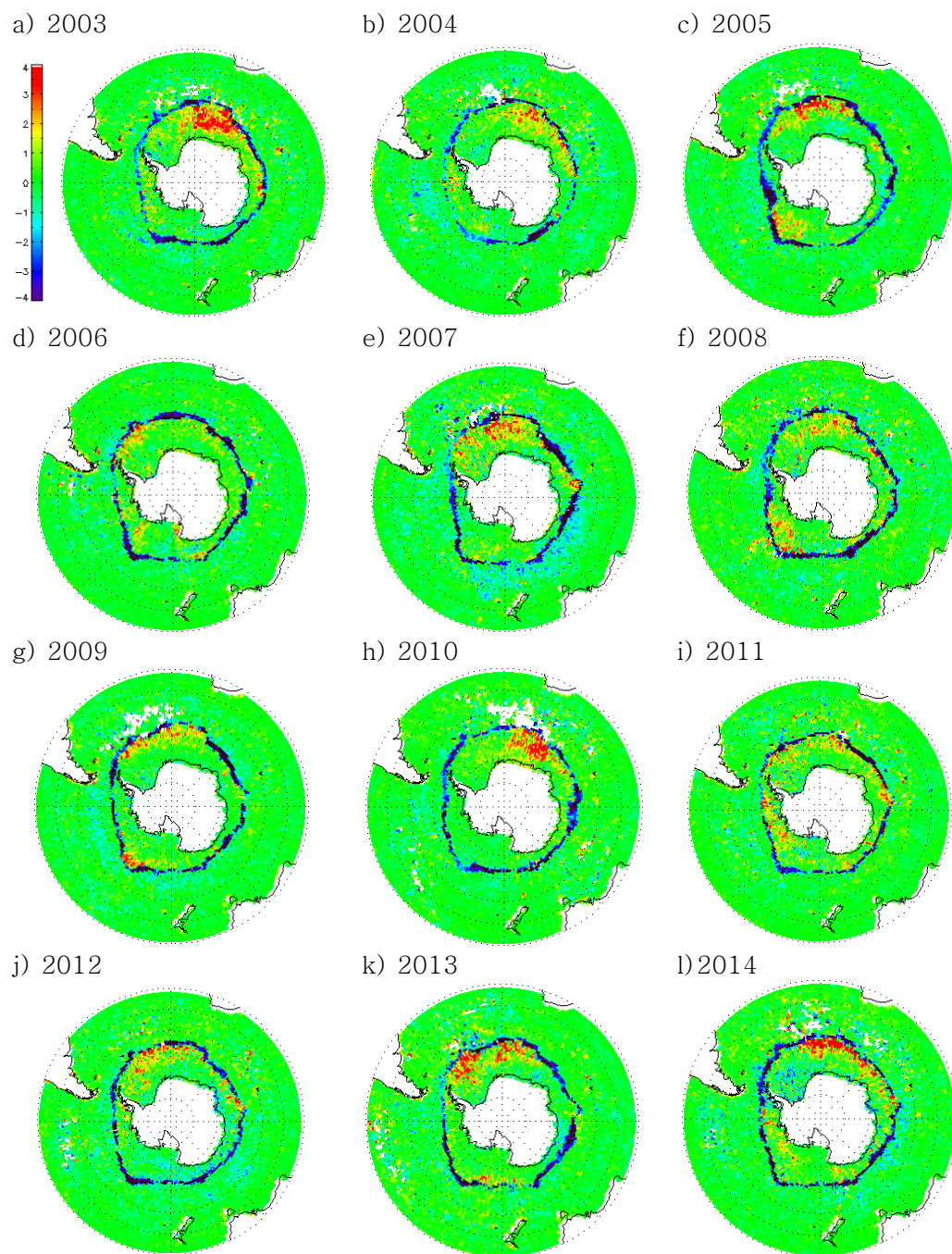


742

743 Fig. 5. Annual-average spatial distributions of the T_{skin} (MODIS) minus T_{skin} (AA_V6) over the
744 southern hemisphere during September 15-23.

745

746

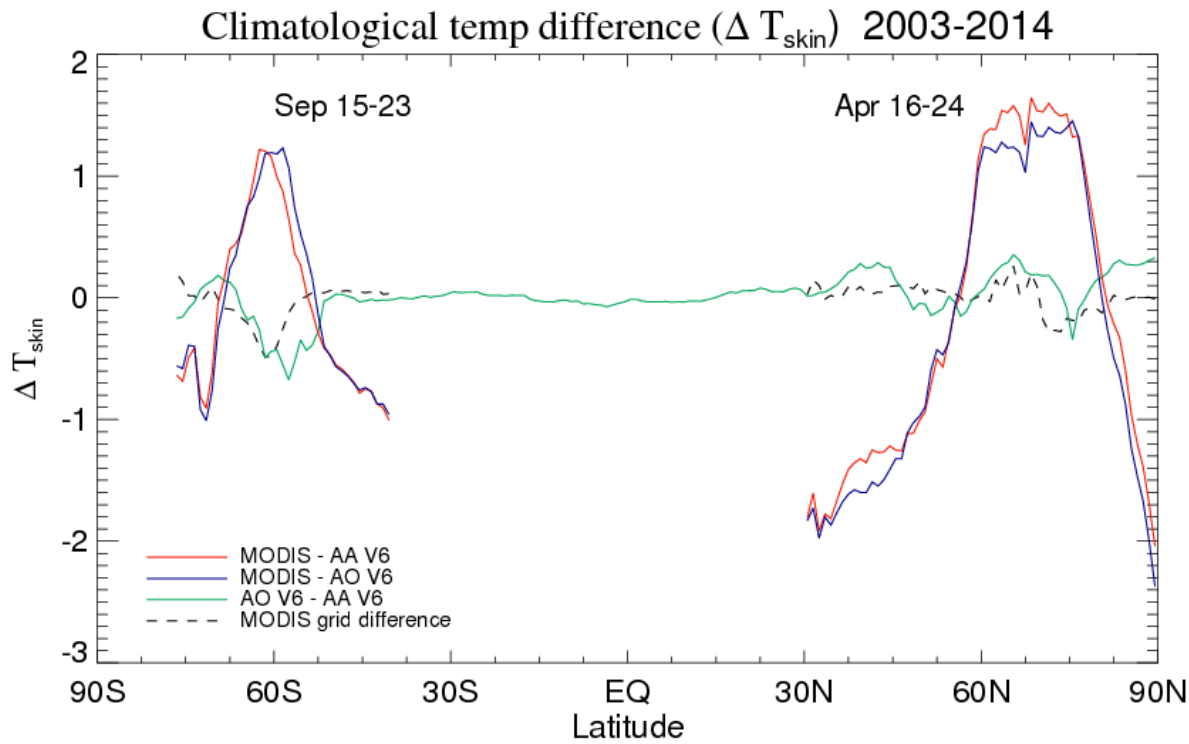


747

748 Fig. 6. Same as Fig. 5 except for $T_{\text{skin}}(\text{AO_V6})$ minus $T_{\text{skin}}(\text{AA_V6})$.

749

750



751

752 Fig. 7. Zonal averaged values of T_{skin} (MODIS) minus T_{skin} (AA_V6) (red solid line), T_{skin} (MODIS) minus T_{skin} (AO_V6) (blue solid line), and T_{skin} (AO_V6) minus T_{skin} (AA_V6) (green solid line). The difference in spatial
 753 grid averages of the MODIS data between 4 km by 4 km and 1° by 1° is shown by the black dashed line. The
 754 difference values are calculated at one degree interval along each latitudinal belt. The climatological data
 755 periods are April 16-24, 2003-2014 over the northern hemisphere, and September 15-23, 2003-2014 over the
 756 southern hemisphere.
 757

758

759

760

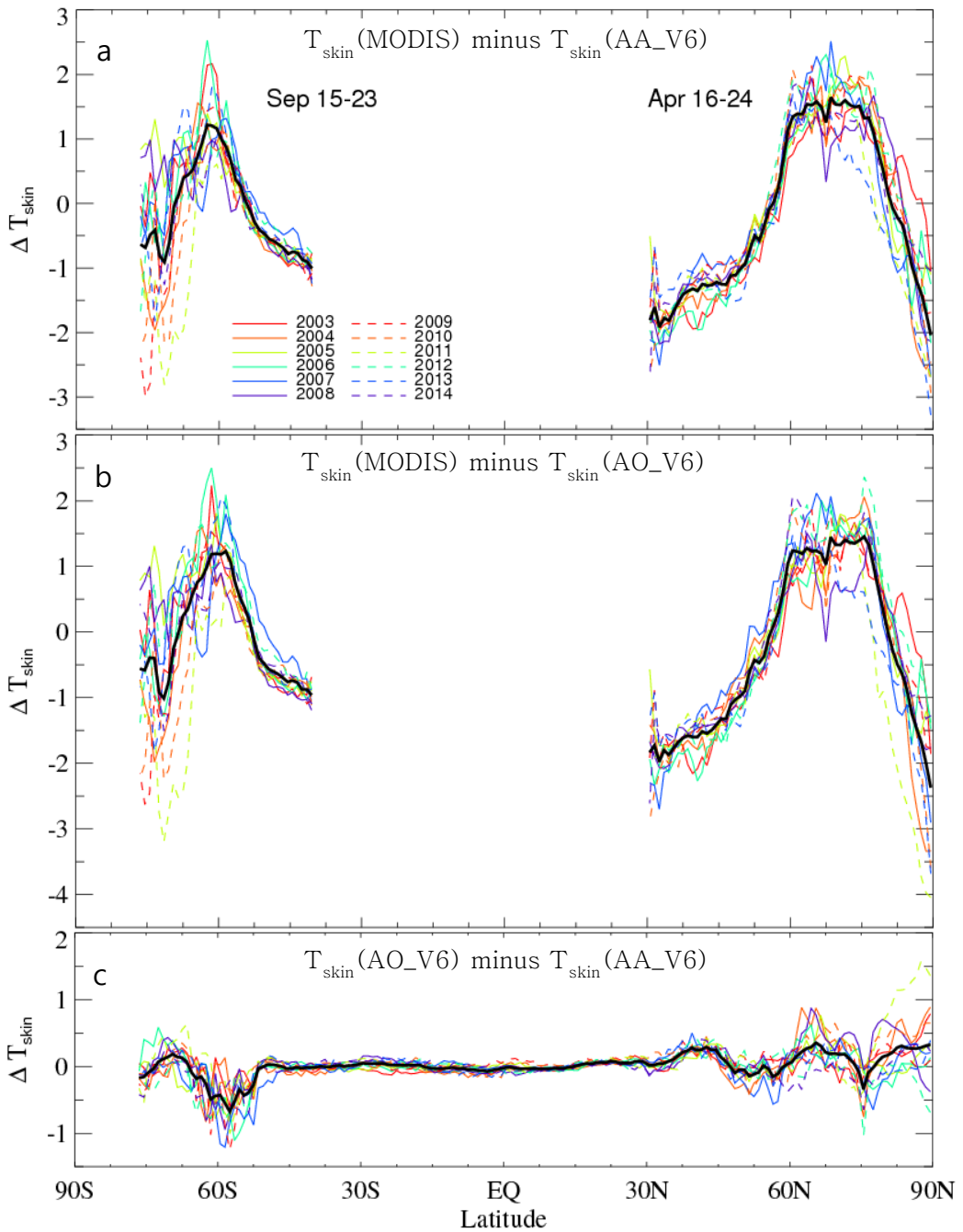
761

762

763

764

765



766

767

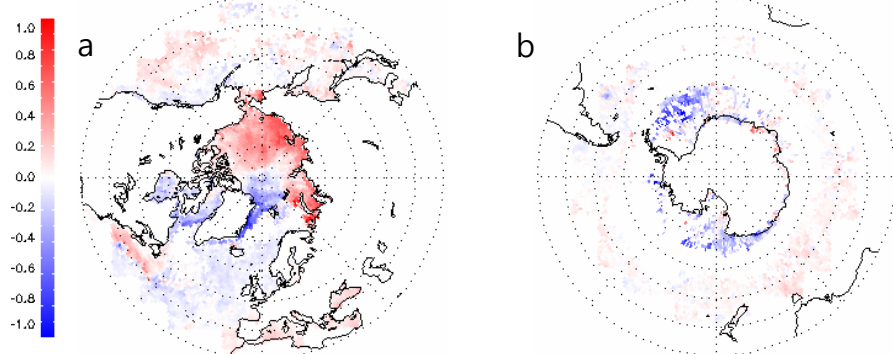
768 Fig. 8. Zonal averaged values of (a) $T_{\text{skin}}(\text{MODIS})$ minus $T_{\text{skin}}(\text{AA_V6})$, (b) $T_{\text{skin}}(\text{MODIS})$ minus $T_{\text{skin}}(\text{AO_V6})$, (c) $T_{\text{skin}}(\text{AO_V6})$ minus $T_{\text{skin}}(\text{AA_V6})$ over the northern hemisphere from April 16 to 24, 2003-2014, and over the southern hemisphere from September 15 to 23, 2003-2014. The values in each year represent the corresponding color lines. The thick black line indicates the mean difference values.

Apr 16-24

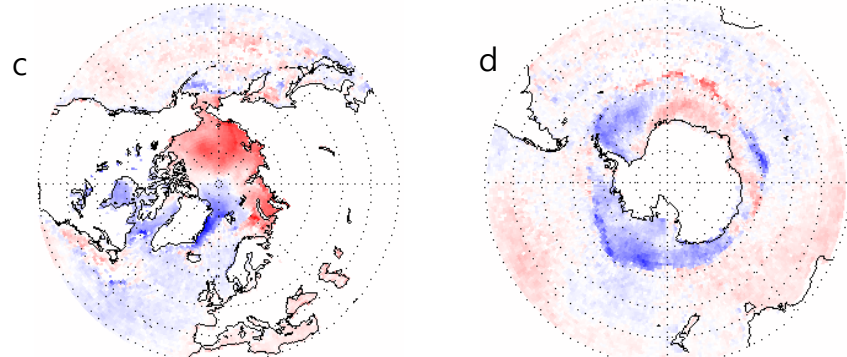
2003-2014

Sep 15-23

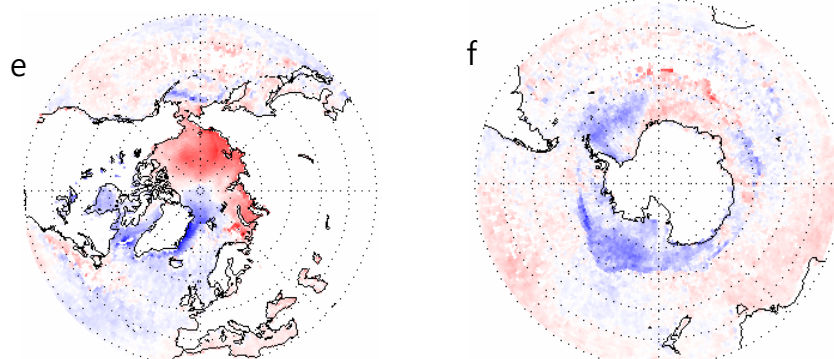
T_{skin} (MODIS)



T_{skin} (AA_V6)



T_{skin} (AO_V6)



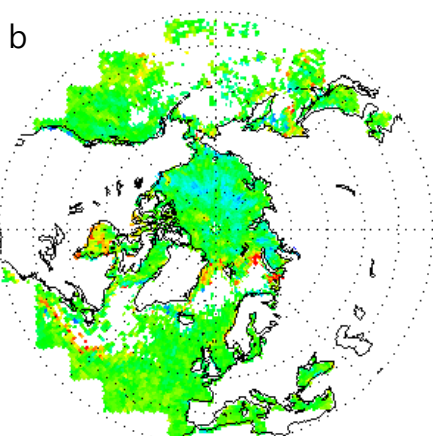
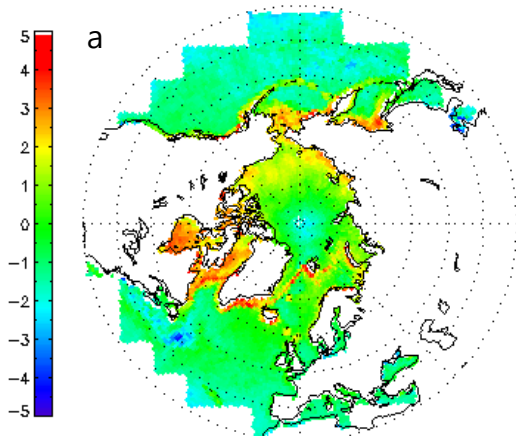
772

773 Fig. 9. Satellite-derived 9-day anomaly trends ($K \text{ yr}^{-1}$) in a grid box of $1^\circ \times 1^\circ$ over the northern hemisphere
774 during April 16-24 of 2003-2014, for the (a) T_{skin} (MODIS), (c) T_{skin} (AA_V6), and (e) T_{skin} (AO_V6), and over
775 the southern hemisphere during September 16-24 of 2003-2014, for the (b) T_{skin} (MODIS), (d) T_{skin} (AA_V6),
776 and (f) T_{skin} (AO_V6).

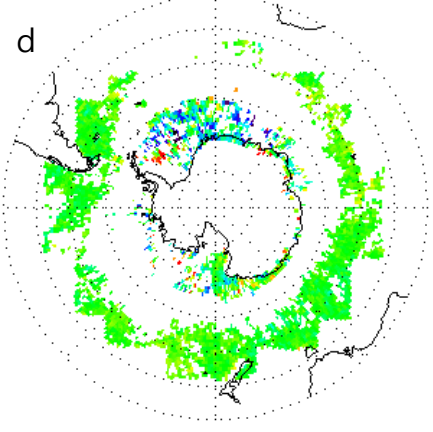
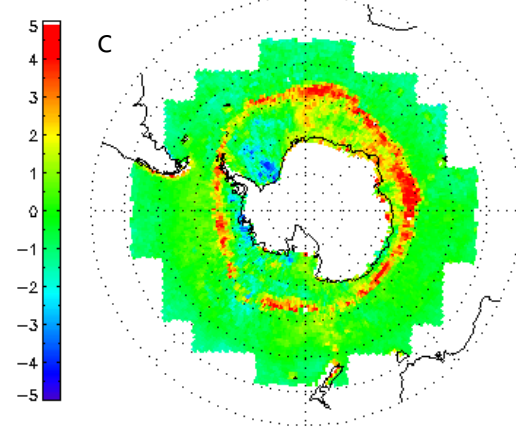
777

 $T_{\text{skin}}(\text{MODIS})$ minus $T_{\text{skin}}(\text{AA_V6})$

Trend difference



778



779

780

781 Fig. 10. (a) 12-year mean of $T_{\text{skin}}(\text{MODIS})$ minus $T_{\text{skin}}(\text{AA_V6})$ (K) over the northern hemisphere
 782 during April 16-24 of 2003-2014, and (b) difference in the thermal trend (K/decade) between T_{skin}
 783 (MODIS) and $T_{\text{skin}}(\text{AA_V6})$. Figures 10c-d are the same as Figs.10a-b except for over the southern
 784 hemisphere during September16-24 of 2003-2014, respectively. Figure 10a is the same as Fig. 3a in
 785 Kang and Yoo (2015).

786

787

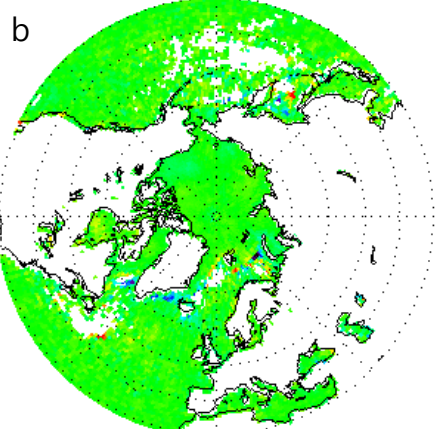
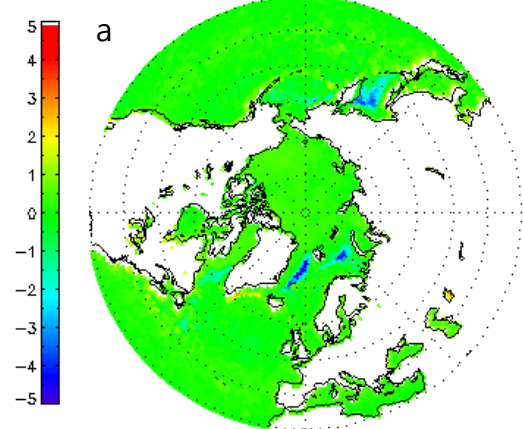
788

789

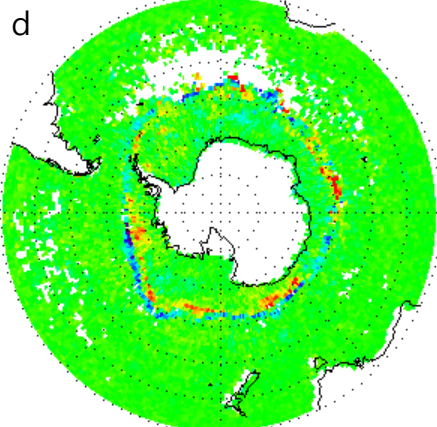
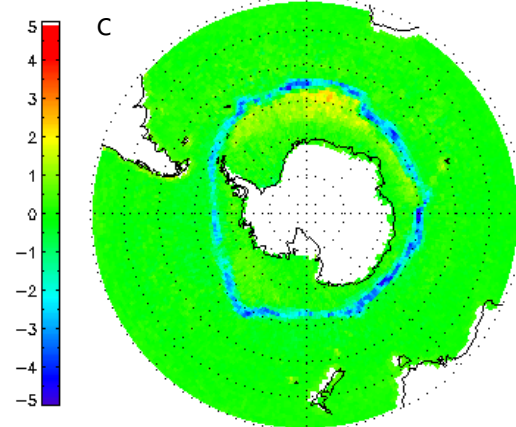
790

 $T_{\text{skin}}(\text{AO_V6})$ minus $T_{\text{skin}}(\text{AA_V6})$

Trend difference



791



792

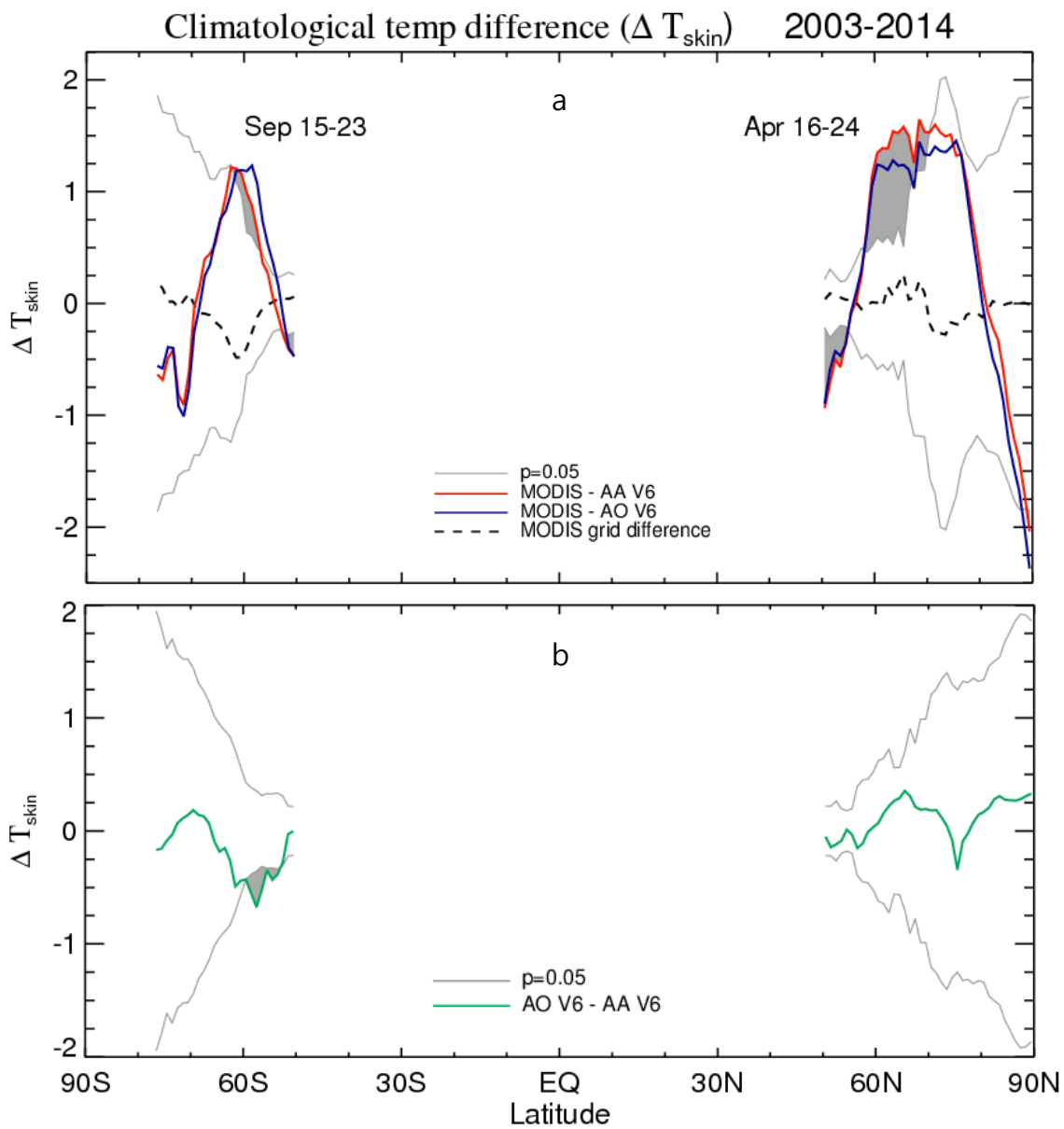
793

794 Fig. 11. Same as Fig. 10 except for $T_{\text{skin}}(\text{AO_V6})$ minus $T_{\text{skin}}(\text{AA_V6})$. Figure 11a is the same as Fig.
795 3c in Kang and Yoo (2015).

796

797

798



799

800 Fig. A1. The difference values (a) between T_{skin} (MODIS) and T_{skin} (AA_V6), and (b) T_{skin} (AA_V6)
 801 and T_{skin} (AO_V6) over a possibly frozen region; shown in Fig. 7. The 5% significance level is
 802 presented as grey solid lines, and the shaded areas are statistically significant at the 0.05 level.

803

804